

N-terminal truncation of *VAPA* leads to disturbed membrane contact sites and syndromic interstitial lung disease in humans

Zoé Grimanelli,¹ Shashank Dadsena,^{2§} Franziska Meichsner,^{2§} Lena Hipp,^{2§} Janathan Altuzar,^{2§} Sophie Abélanet,¹ Felix Marbach,³ Frédéric M. Vaz,⁴ Özge Altug-Teber,⁵ Oliver Brandau,⁵ Ana Rita Dias Araújo,¹ Clara Pradelli,¹ Romain Gautier,¹ Simone Reu-Hofer,⁶ Christian Mühlfeld,⁷ Morten Kampelmann,⁷ Marcus Höring,⁸ Gerhard Liebisch,⁸ Susanne Hämmerling,⁹ Xiahua Yang,¹⁰ Julian Warfsmann,¹⁰ Maja Hempel,² Dorothea Haas,¹¹ Matthias Griesse,¹⁰ Bruno Mesmin,^{1*} and Matias Simons^{2*}

¹ Université Côte d'Azur, Inserm, CNRS, UMR 7275, Institut de Pharmacologie Moléculaire et Cellulaire, 660 route des lucioles, Valbonne, France

² Institute of Human Genetics, Medical Faculty, University of Heidelberg, Heidelberg, Germany

³ Institute of Human Genetics, Medical Faculty, University of Bonn and National Center for Hereditary Tumour Syndromes, University Hospital Bonn, Germany

⁴Amsterdam UMC location University of Amsterdam, Core Facility Metabolomics, Department of Laboratory Medicine, Laboratory Genetic Metabolic Diseases, Emma Children's Hospital, Amsterdam, The Netherlands.

⁵ Synlab GmbH, MVZ Humangenetik Mannheim, Germany

⁶ Institute of Pathology, University of Würzburg, Würzburg, Germany

⁷ Institute of Functional and Applied Anatomy, Hannover Medical School, Biomedical Research in Endstage and Obstructive Lung Disease Hannover (BREATH), Member of the German Center for Lung Research (DZL), Hannover, Germany

⁸ Institute of Clinical Chemistry and Laboratory Medicine, University Hospital of Regensburg, Regensburg, Germany

⁹ Division of Pediatric Pneumology and Allergology, Department of Pediatrics III, Medical Faculty, University of Heidelberg, Heidelberg, Germany and Translational Lung Research Center Heidelberg (TLRC), German Center for Lung Research (DZL), Heidelberg, Germany

¹⁰ Department of Pediatric Pneumology, Dr. von Hauner Children's Hospital, Ludwig-Maximilians University, German Centre for Lung Research (DZL), Munich, Germany

¹¹ Heidelberg University, Medical Faculty of Heidelberg, Department of Pediatrics I, Division of Metabolic Diagnostics and Neonatal Screening, Heidelberg, Germany

[§] These authors contributed equally

*Correspondence: mesmin@ipmc.cnrs.fr (B.M.), Matias.Simons@med.uni-heidelberg.de (M.S.)

Abstract

VAP proteins form membrane contact sites between the endoplasmic reticulum and other organelles through their interaction with FFAT-containing proteins. These contact sites enable coordinated lipid synthesis, transfer and metabolism in cells. However, their tissue-specific functions remain largely unexplored. Here, we report the first patient with a homozygous nonsense variant in the *VAPA* gene (p.(Glu12*)), exhibiting profound global developmental delay and progressive surfactant dysfunction phenotype leading to cholesterol pneumonitis and pulmonary fibrosis. . The variant leads to an N-terminal truncation with limited FFAT binding capacity. In alveolar type-II cells of the lung, VAPA deficiency results in impaired lamellar body formation. Specifically, we identified the pulmonary disease-associated protein ABCA3, which is a key player for surfactant lipid buildup in lamellar bodies, as a new VAPA interactor. The VAPA-ABCA3 interaction promoted lipid exchange within previously uncharacterized ER-LB MCS, a function not supported by the N-terminal truncation. Altogether, our results identify compromised VAPA-dependent MCS function as a disease mechanism for syndromic lung disease, thereby revealing a new pathway for surfactant lipid trafficking.

1 Introduction

2 Membrane contact sites (MCS) play a crucial role in facilitating non-vesicular transport of lipids,
3 calcium fluxes and various signaling events between organelles¹⁻³. These sites are characterized
4 by the close apposition of two organelle membranes without fusion. Numerous protein families,
5 including the vesicle-associated membrane protein-associated protein (VAP) family, are involved
6 in this process^{4,5}. The VAP family comprises VAPA, VAPB, and motile sperm domain-containing
7 proteins 1-3 (MOSPD 1-3)^{6,7}. These proteins share common features, including a C-terminal
8 transmembrane domain embedded into the endoplasmic reticulum (ER) membrane, and a
9 cytosolic N-terminal major sperm protein (MSP) domain. The MSP domain binds to specific motifs,
10 such as two phenylalanines in an acidic tract (FFAT), and FFAT-related motifs in other proteins⁸⁻
11 ¹⁰. VAPA and VAPB (collectively referred to as VAPA/B) form MCS between the ER and nearly all
12 organelle-limiting membranes^{11,12}. As reported in the IntAct database, VAPA/B have at least 350
13 interaction partners¹³. A well-characterized MCS is between the ER and the *trans*-Golgi network
14 (TGN) mediated by the MSP domain of VAPA and the FFAT motif of Oxysterol-binding protein
15 (OSBP), which facilitates the exchange of cholesterol and phosphatidylinositol-4-phosphate
16 (PI4P)^{14,15}. Tissue-specific functions of VAPA and VAPB, and the MCS they participate in, remain
17 largely unexplored.

18 While pathogenic variants in *VAPB* cause amyotrophic lateral sclerosis (ALS)-type 8, as
19 well as a specific form of late-onset spinal muscular atrophy^{16,17}, *VAPA* variants have not yet been
20 associated with human diseases. Interestingly, complete *VAPA* deficiency is embryonic lethal in
21 mice, whereas deletion of *VAPB* is compatible with survival into adulthood^{18,19}. The difference in
22 the tolerance to the knockout of each of the paralogues could be due to the higher abundance of
23 VAPA in most tissues¹¹, so that its absence results in a larger reduction of the total VAP pool than
24 does *VAPB* deletion; alternatively or in addition, the different sensitivity could be due to the
25 existence of an essential function of VAPA that VAPB cannot carry out.

26 Here, we report the first patient with a homozygous nonsense variant in the *VAPA* gene.
27 The clinical picture is a severe multi-system disorder with a progressive lung disease with

lipoproteinous alveolar filling developing into pulmonary fibrosis as predominant manifestation, thereby suggesting an important role of VAPA in lung health. We show that the variant leads to an N-terminal truncation deleting more than half of the MSP domain. This truncated MSP domain, predicted to be unstable, exhibits limited capacity to bind FFAT motifs and form MCS. By examining the role of VAPA in lamellar body (LB) formation and surfactant buildup in LBs of alveolar type-2 (AT2) cells, we identified the membrane-spanning ATP-binding cassette transporter A3 (ABCA3) as a new VAPA interactor. Overall, our study links a clinical case to a new function of VAPA in lung cells, where it participates in the formation of previously uncharacterized MCSs and in a lipid transport pathway that contributes to pulmonary surfactant homeostasis.

Results

Clinical description of the patient

The female patient was born to healthy non-consanguineous parents after an uncomplicated pregnancy via secondary Caesarean section at term (41+1 weeks of gestational age) with low body weight (2400 g, -2.70 SDS), height (47 cm, -2.37 SWD) and head circumference (32 cm, -2.48 SDS) and normal postnatal adjustment (APGAR 10/10). At 2.5 months an ophthalmological examination was performed because of lack of eye contact, which revealed congenital amaurosis with abnormal retinal pigmentation and missing responses in electroretinogram. Cranial MRI showed mild microphthalmia but no morphologic correlate for the impaired vision. Molecular analysis for genes causing Leber congenital amaurosis did not reveal specific abnormalities. An extensive work-up was initiated at the age of 3.5 years because of profound global developmental delay (no speech, free sitting was possible, but no standing position), severe dystrophy (weight 8,4 kg, -5.23 SDS, height 82 cm, -5.03 SDS, BMI 12.49, -2.56 SDS) and progressive microcephaly (head circumference 43,3 cm, -6.3 SDS). Physical examination showed facial dysmorphism (deep set eyes with narrow interocular distance, low set ears, prominent nose, tent-shaped mouth, microretrognathia), atopic dermatitis with perioral eczematous lesions ([Figure 1A](#)), severe

1 muscular hypotonia with kyphosis of the thoracic spine and funnel chest, clubbing of fingers and
2 toes (Figure 1B) as well as mild hepatomegaly.

3 Laboratory showed increased aminotransferases and grossly elevated lactate
4 dehydrogenase (1019 U/L). Metabolic studies remained unremarkable, including sterols,
5 peroxisomal and lysosomal diagnostics. Abdominal echography revealed slight hepatomegaly
6 with inhomogeneous tissue and normal fibroelastography, splenomegaly and bilateral 2°
7 nephrocalcinosis. In the echocardiography, slightly increased right ventricular pressure (30 mm
8 Hg) was observed. As chest X-ray showed a fine reticular pattern pointing to interstitial lung
9 disease, high resolution chest CT revealed diffuse bilateral ground-glass opacities (GGO) with
10 inter- and intralobular septal thickening and reticulation (crazy paving pattern) (Figure 1C). A
11 diagnostic bronchoalveolar lavage (BAL) confirmed the diagnosis of pulmonary alveolar
12 proteinosis (PAP), revealing milky lavage return and abundant extracellular, PAS positive debris,
13 oval bodies and foamy macrophages on cytology. Therapeutic whole lung lavages were initiated,
14 the first five improved oxygenation and removed substantial protein from the lungs, however with
15 ongoing disease lavage efficacy was lost (Figure S1E).

16 Lipidomic analysis of lung lavage fluids was characteristic for PAP, including a marked
17 overall increase in total lipid mass compared to controls (Figures S1A and S1B). The main
18 surfactant lipid phosphatidylcholine (PC; mainly PC 32:0) was moderately reduced, whereas free
19 cholesterol (FC) was slightly increased (Figure 1D). By contrast, cholesterol ester (CE) levels were
20 remarkably high (mainly due to CE 16:0), accounting for more than 25% of total lipids in the BAL
21 (Figures 1D and S1A), which distinguished this case from typical PAPs. Histology showed lung
22 tissue with alveolar hypoplasia, many alveoli were filled with proteinaceous eosinophilic material
23 consistent with PAP but contained unusual large numbers of cholesterol clefts and foam cells.
24 There was interstitial fibrosis with increase in interstitial collagen and hyperplastic AT2
25 pneumocytes (Figure 1E). In a subset of AT2 cells, LB were of abnormal appearance. This was
26 confirmed and quantified by transmission electron microscopy (TEM), showing that 32.7% of all
27 LB in 150 AT2 cells from five samples have amorphous dense cores that are rarely seen in control

1 samples (Figures 1F and S1C). Large cholesterol clefts surrounded by cellular debris or
2 multilamellar lipid sheets were also observed in the alveolar space by TEM (Figure S1D).

3 The further course of the disease was complicated by increasing oxygen demand and
4 tachypnea (1.5 l/min to reach an oxygen saturation of 95 to 98%), which did not improve on high
5 dose corticosteroid therapy. Therapeutic whole lung lavages for PAP were less and less beneficial
6 due to a rapidly developing progressive pulmonary fibrosis which dominated the clinical course
7 (Figure S1E). Anti-inflammatory therapy with azithromycin and modulation of surfactant lipid
8 metabolism by consecutive administration of fish oil, rosuvastatin and PPAR γ activation by
9 pioglitazone could not prevent progressive global respiratory insufficiency, leading to death at the
10 age of 5.5 years due to sepsis and cardiac arrhythmia.

12 Exome sequencing identifies a homozygous *VAPA* variant

13 Exome sequencing identified a homozygous nonsense variant in the *VAPA* gene (c.34G>T;
14 p.(Glu12*)), which was confirmed by Sanger sequencing (Figure 1G). Segregation analysis
15 identified the variant in the mother in the heterozygous state (Figure 1G), while the father's DNA
16 showed a wildtype pattern. Trio exome analysis of chromosome 18 revealed isodisomy for the
17 *VAPA*-containing chromosome area 18p11.22-18q12.1, assuming a partial trisomy 18 after
18 meiotic crossing over with subsequent rescue and loss of the paternal chromosome in the first cell
19 division of the fertilized egg^{20,21}. In the isodisomy region no other disease-relevant variants were
20 detected apart from the *VAPA* variant, which was also found to be absent from population
21 databases (e.g. gnomAD). Moreover, in the exome analysis, no pathogenic variants in other genes
22 associated with PAP (*SFPC*, *SFPB*, *ABCA3*, *NKX2.1*, *FOXF1*, *FLNA*, *CSF2RA*, *CSF2RB*, *GATA2*,
23 *SFTPA1/2*, *SLC7A7*, *CCR2*, *IL3*, *STAT5B*, *MARS1*, *SMPD1*, *NPC1/2*) could be found.

25 *VAPA*-Glu12* variant leads to N-terminally truncated proteins via downstream alternative 26 start codons

1 To functionally validate the variant, primary skin fibroblasts were obtained through a skin biopsy.
2 First, the consequences of the VAPA-Glu12* variant were investigated on mRNA and protein level.
3 Typically, nonsense mutations before the last exon induce nonsense-mediated mRNA decay
4 (NMD), which prevents translation to protect cells from possibly harmful truncated proteins²².
5 Strikingly, however, no change in *VAPA* mRNA levels was observed in VAPA-Glu12* fibroblasts
6 compared to control fibroblasts, as assessed by qPCR (Figure 2A), indicating that the mutant
7 mRNA evades NMD. To study the effect on protein levels, Western blotting using protein lysate of
8 both control and VAPA-Glu12* fibroblasts was performed. Interestingly, VAPA-Glu12* fibroblasts
9 showed no band at the expected molecular weight for VAPA (28 kDa) but instead displayed a band
10 at a lower molecular weight (~18 kDa), along with a faint additional band detected at an even
11 lower weight (~16 kDa) (Figure 2B). The two bands did not match the protein fragment expected
12 from a translation up to the premature stop codon, which would produce a peptide of around 1
13 kDa. Moreover, they were visible with two antibodies with two different epitopes, arguing against
14 unspecificity. VAPB mRNA and protein levels were unaltered in the patient cells, suggesting no
15 compensatory upregulation (Figure 2B). Immunofluorescence (IF) labeling showed a diffuse ER
16 localization of VAPA in control and patient fibroblasts, while VAPB was mislocalized to distinct ER
17 subdomains in the patient cells (Figures 2C and S2C).

18 We hypothesized that the shorter VAPA form in the patient cells might stem from an
19 alternate start codon downstream of the mutation that reinitiates translation, giving rise to an N-
20 terminal truncated protein (Figure 2D). Based on the size of the VAPA protein fragment detected
21 in the VAPA-Glu12* fibroblasts, three possible in-frame start codons downstream of the mutation
22 were identified, hereafter referred to as M79, M96 and M109. Translation reinitiation at these
23 codons would yield truncated VAPA variants of calculated molecular weights of 19.4 kDa, 17.3
24 kDa, and 15.9 kDa, respectively. To test whether any of these start codons could generate the short
25 form of VAPA, wild-type (WT) VAPA and full-length *VAPA* cDNA from patient fibroblasts was
26 cloned into a plasmid carrying a 2xFLAG-tag and expressed in RPE-1 VAPA KO cells. Western blot
27 analysis of cell lysates with an anti-FLAG antibody revealed a distinct lower band when patient-

1 derived cDNA was used, compared to WT cDNA, with a size shift corresponding to the one
2 previously observed with primary fibroblasts (Figure S2D). Moreover, an additional lower faint
3 band was visible, which was also detected in VAPA-Glu12* fibroblast lysate. As the 2xFLAG-tag is
4 C-terminal, this demonstrates that the C-terminal part of VAPA is still expressed. To prove that
5 these bands result from translation reinitiation at an alternate start codon downstream of the
6 VAPA-Glu12* mutation and to identify which codon specifically resulted in the truncated band,
7 the three possible downstream start codons were mutated to code for glycine instead of
8 methionine. The resulting plasmids were again used to transfect RPE-1 WT and VAPA KO cells,
9 which were consecutively analyzed by Western blotting (Figure 2E). While M96G did not affect
10 the band pattern, the expression of M109G led to the expression of multiple bands at even lower
11 molecular weights. The stronger upper band was absent in cells expressing the VAPA-Glu12*-
12 M79G transcript, indicating that M79 is the main alternative start codon. Analysis of the sequence
13 around this start codon confirmed that it matches the consensus Kozak sequence²³, except for
14 position +4, where there is a cytosine instead of the conserved guanine (Figure S2E).

15 In summary, these data suggest that the nonsense mutation VAPA-Glu12* leads to N-
16 terminal truncations mediated by the reinitiation of translation at the alternate, downstream start
17 codons M79 and, to some extent, M109. The most prominent fragment misses the amino acids 1-
18 78 (from here on termed VAPA Δ 78). Since the MSP domain lies between amino acids 14 to 131²⁴,
19 we hypothesized that VAPA Δ 78 has a dysfunctional MSP domain while remaining anchored to the
20 ER membrane.

21

22 **Molecular dynamics (MD) simulations predict an unstable MSP domain in VAPA Δ 78 with** 23 **limited FFAT binding capacity**

24 To gain structural and functional insights into the MSP domain of VAPA Δ 78 (hereafter MSP Δ 78),
25 we conducted *in silico* analyzes using molecular dynamics (MD) simulations. Compared with MSP
26 WT (PDB: 2RR3), which adopts a seven-stranded immunoglobulin-like β sandwich and one α
27 helix, the AlphaFold2-based model of MSP Δ 78 is severely truncated, containing only two β strands

1 and one α helix (Figure 3A). MSP Δ 78 notably lacks the conserved VAP consensus sequence (VCS;
2 aa. 42-63), known to mediate FFAT binding²⁵. The MSP Δ 78 model was simulated for 500 ns (in
3 120 mM NaCl, 310 K) and compared with MSP WT. Unlike MSP WT, MSP Δ 78 underwent
4 pronounced structural rearrangements, producing a more compact molecule. Backbone C $_{\alpha}$ root
5 mean square deviation (RMSD) analysis revealed that this structural transition occurred within
6 the first 100 ns and indicated a reduced overall stability of MSP Δ 78 compared to MSP WT (Figure
7 3A).

8 The VAPA MSP–FFAT complex is stabilized by electrostatic, hydrophobic, and hydrogen-
9 bond (H-bond) interactions²⁶, with a large positively charged MSP surface binding negatively
10 charged FFAT motifs (Figure 3B). By contrast, MSP Δ 78 lacks a distinctive positively charged
11 region, which could compromise FFAT binding (Figure 3C). This prompted us to examine
12 interactions between MSP Δ 78 and the archetypical FFAT motif of OSBP during simulation, and to
13 compare them with MSP WT (Figure S3A; Videos S1 and S2).

14 As expected, the MSP WT–FFAT complex was highly stable, with electrostatic interactions
15 contributing predominantly (64%) to the binding energy (-693.3 kJ.mol⁻¹) (Figures 3D and 3E).
16 By comparison, the MSP Δ 78–FFAT complex, built from the final MSP Δ 78 structure obtained by
17 the simulation shown in Figure 3C, adopted multiple conformations, suggesting reduced stability,
18 although residual interaction persisted. Electrostatic contributions dropped to 40.7% of the total
19 interaction energy (-230.8 kJ.mol⁻¹). H-bond analysis showed that MSP residues 43-57 formed the
20 most stable contacts with FFAT (Figure 3F and S3B), a region largely overlapping the VCS and
21 absent in MSP Δ 78. Although new H-bonds formed with MSP Δ 78, they were less stable than in the
22 WT complex (Figure 3G). Consistently, MSP Δ 78 formed much fewer close (< 4 Å) and persistent
23 intermolecular contacts with FFAT over 1 μ s simulations (Figure 3H).

24 Next, to assess whether truncating the first 78 residues of VAPA impacted FFAT binding
25 *in vitro*, we mixed the membrane-tethering region of OSBP (OSBP[1-408]) with PI4P-containing
26 liposomes and either VAPA[8-230] or VAPA[79-230] construct, followed by sucrose gradient
27 flotation (Figure 3I). Only VAPA with an intact MSP associated with liposome-bound OSBP[1-408]

(Figures 3J and 3K), whereas VAPA[79-230] was retrieved in the bottom fraction. As a control, addition of excess FFAT peptide displaced VAPA[8-230], confirming that its binding depends on MSP–FFAT interaction.

Overall, simulations and *in vitro* assays revealed that VAPA truncation profoundly alters MSP structure and compromises FFAT binding. MSP Δ 78 is predicted to be intrinsically unstable with a modified electrostatic surface, preventing it from maintaining close contact with FFAT over time. Consistently, a VAPA construct lacking the first 78 residues failed to bind OSBP[1-408] *in vitro*.

Patient fibroblasts exhibit VAPA KO phenotypes

To study the functional consequences of the unstable MSP domain at the cellular level, we first tested whether VAPA-Glu12* fibroblasts display typical phenotypes of VAPA KO cells. We previously demonstrated that VAPA facilitates lipid exchange at ER-Golgi MCSs mediated by OSBP and CERT, while also playing a significant role at ER-mitochondrial MCSs by enhancing the accumulation of cardiolipin in mitochondria and supporting mitochondrial fusion²⁷. Accordingly, VAPA KO cells exhibited more OSBP and CERT at the TGN due to increased PI4P levels in this organelle, as well as a drastically altered mitochondrial morphology, with mitochondria appearing more circular rather than having their typical elongated shape²⁷. Therefore, the subcellular distribution of OSBP and CERT in VAPA-Glu12* and control fibroblasts was first investigated by immunofluorescence staining (Figures 4A and 4B). Compared to control fibroblasts, both OSBP and CERT levels were significantly elevated at the TGN (marked by TGN46) in VAPA-Glu12* fibroblasts, indicating impaired PI4P exchange between ER and TGN. As PI4P is exchanged with cholesterol, excess cholesterol in the ER can lead to esterification and storage in lipid droplets (LD)²⁸. To assess this, we examined LD and quantified neutral lipids in patient and control fibroblasts using cell imaging and high-performance liquid chromatography-mass spectrometry (HPLC-MS), respectively. While LD number and size was higher in VAPA-Glu12* fibroblasts than

1 in controls, HPLC-MS revealed a strong accumulation of CE together with an increase of other
2 neutral lipids, such as triacylglycerol (TG) and ether-linked TG (TG[O]) (Figures 4C and 4D).

3 Next, the shapes of mitochondria in VAPA-Glu12* vs. control fibroblasts as well as RPE1
4 WT vs. KO cells were studied using Mitotracker and quantified using a form factor, for which a
5 value of 1 reflects a round morphology. Interestingly, while in control fibroblasts and in RPE1 WT
6 cells the values were around 0.25, in VAPA-Glu12* fibroblasts and RPE1 KO cells the values were
7 elevated (0.4 and 0.7, respectively). Thus, the mitochondria of the patient fibroblasts are more
8 circular than controls but not as circular as in RPE1 KO cells (Figures 4E and 4F). IF further
9 revealed that VAPB-positive ER subdomains in VAPA-Glu12* fibroblasts colocalized with the
10 circular mitochondria (Figure S2B). In summary, phenotypes typical for VAPA KO cells are also
11 present in VAPA-Glu12* fibroblasts.

13 **N-terminally truncated VAPA cannot rescue VAPA KO RPE1 cells**

14 To study whether VAPA Δ 78 can rescue VAPA KO phenotypes, we transiently transfected EGFP-
15 VAPA WT or EGFP-VAPA Δ 78 into VAPA KO RPE1 cells and quantified OSBP distribution and
16 mitochondria phenotypes. We observed that EGFP-VAPA WT expression fully restored the
17 cytosolic localization of OSBP, whereas the VAPA Δ 78 construct did not (Figures 4G and 4H).
18 Strikingly, the levels of OSBP at the TGN in EGFP-VAPA Δ 78 transfected cells remained as high as
19 in non-transfected cells. These results indicate that VAPA Δ 78 is unable to support OSBP activity
20 and are consistent with the defective interaction between MSP Δ 78 and OSBP FFAT as
21 demonstrated in Figure 3J. Accordingly, expressing EGFP-VAPA WT but not EGFP-VAPA Δ 78 in
22 VAPA KO RPE-1 cells converted most of the large spherical mitochondria stained with Mitotracker
23 red into thin and elongated ones (Figures S4A and S4B). Taken together, these results indicate
24 that the p.(Glu12*) mutation produces a truncated VAPA protein that is no longer a functional
25 partner for important proteins linked to lipid transport at ER-Golgi MCS and ER-mitochondria
26 MCS.

VAPA deficiency leads to lamellar body defects in an AT2-derived cell line

Finally, we addressed the contribution of VAPA deficiency to the patient phenotype by focusing on PAP as the most severe organ manifestation. Therefore, we inactivated VAPA in A549 cells, which are derived from AT2 cells. These cells form LBs, which are the organelles where the surfactant is synthesized. Previously, it was shown that LB formation can be boosted via the overexpression of ABCA3, the key phospholipid transporter in the LB membrane, which also helps reduce cell cholesterol via surfactant secretion²⁹. Therefore, we transiently transfected ABCA3-mCherry in control or VAPA KO A549 cells for 24 h, and assessed the uptake of BODIPY-labeled PC and cholesterol into LBs using wide-field fluorescence imaging (Figures 5A-D). Our data showed that VAPA deficiency does not impair ABCA3-induced formation of LBs, as LBs in VAPA KO cells accumulated BODIPY-C16-PC at levels comparable to those in control cells (Figures 5A and 5C). By contrast, the ABCA3 E690K mutant, known to disrupt the coupling between ATPase activity and lipid transport³⁰, largely prevented this accumulation. Next, we performed Filipin staining to quantitatively assess FC amounts in LBs induced by the expression of ABCA3-mCherry in control and VAPA KO cells. In this case, significantly less cholesterol accumulated in LBs of VAPA KO cells than in controls (Figures 5B and 5D), suggesting that a “VAPA-ABCA3” pathway contributes to FC enrichment in LBs.

Investigating the underlying mechanism of this pathway further, we noticed that ABCA3 comprises a putative FFAT motif in its sequence (res. 511 EKALRNEYFEAEPED), with a calculated score of 2.5, suggesting that it could be functional for VAP binding³¹ (Figures S5A and S5B). At the structural level, the FFAT-like motif is located in an unfolded loop of ABCA3, which is accessible from the cytosol (Figures 5E and S5C). If VAPA and ABCA3 proteins interact directly, we expect them to populate MCSs between the ER and LBs. However, such ER-LB contacts have not been described previously. To test this, we co-transfected cells with ABCA3-mCherry and Halo-tagged (HTN) VAPA constructs, labeled them with a Halo-reactive Janelia Fluor 646 dye before imaging with τ -STED super-resolution microscopy. This revealed clear ER-LB contact regions, where VAPA and ABCA3 co-localized (Figure 5F). By contrast, HTN-VAPAA78 failed to accumulate at these sites

1 when co-expressed with ABCA3-mCherry in VAPA KO A549 cells, indicating that an intact MSP
2 domain is required. Similarly, an ABCA3 FFAT mutant, comprising the point mutations
3 Y524A/F525A (ABCA3^{YF>AA}-mCherry), did not co-enrich with HTN-VAPA at MCS. Together, these
4 results indicate that an MSP-FFAT interaction between VAPA and ABCA3 promotes their
5 recruitment at ER-LB MCS. Next, we repeated the filipin experiments described above with
6 transfections of either EGFP-VAPAA78 or ABCA3^{YF>AA}-mCherry, in comparison with WT
7 constructs, in VAPA KO cells. Our results indicated that, when the interaction determinants are
8 impacted, either via a defective FFAT in ABCA3 or by the disease-related truncation of the MSP
9 domain of VAPA, then much less FC accumulates in LBs (Figures 5G and 5H). We also observed
10 that the expression of ABCA3^{YF>AA}-mCherry caused a modest but statistically significant reduction
11 in BODIPY-C16-PC incorporation into LBs, suggesting a contributory role of ER-LB MCS also to
12 the transport of PC, which is the main surfactant constituent. (Figures 5A and 5C).

13 In summary, our results indicate that VAPA and ABCA3 form a functional pair at ER-LB
14 MCS, promoting the accumulation of cholesterol and possibly other lipids within LBs. Lipid
15 transfer to LB, which is a key step in surfactant formation, is affected in cells expressing the
16 predominant truncated protein derived from VAPA p.(Glu12*) mutation, suggesting that a defect
17 in lipid transfer at ER-LB MCS could contribute to the pulmonary phenotype found in the disease
18 (Figure 5I).

20 Discussion

21 Here, we report a patient with a multi-system disease due to a homozygous nonsense variant in
22 the *VAPA* gene. The phenotype consists of congenital retinal blindness, progressive failure to
23 thrive and microcephaly, atopic dermatitis, profound global developmental delay and oxygen-
24 dependent interstitial lung disease due to PAP. On the molecular level, we show that the nonsense
25 variant leads to N-terminal truncations due to usage of alternative start codons, in particular M79
26 (Figure 2E). This mechanism has been previously described, but so far only rarely in human
27 genetic studies^{23,32-35}. Yet, it is very likely that this mechanism is at play whenever nonsense

1 variants cause a milder phenotype than expected for a loss-of-function mutation, independently
2 of any genetic modifiers. It is therefore possible that survival with VAPA loss-of-function is
3 normally not possible beyond embryonic stages as shown in the mouse model. We assume that in
4 our patient any residual function of the N-terminal truncation, and possibly additional genetic or
5 environmental factors, led to abnormally long survival. While we found that the N-terminal
6 truncation abolished FFAT binding and failed to rescue organellar phenotypes in the VAPA KO
7 RPE1 cells, we cannot rule out that in the whole organismal setting there might be some residual
8 functions of truncated VAPA or partial compensation by VAPB. By contrast, VAPB KO mice are
9 viable and fertile, suggesting that VAPA can compensate for loss of VAPB.

10 VAPs play a crucial role in various cellular processes, including organelle membrane
11 tethering, lipid transfer, autophagy, ion homeostasis, and defense against viral infections⁶. Many
12 VAP interactors have been identified, together mediating the contact between the ER and different
13 organelles. In our previous work, we found that thanks to its flexibility, VAPA can function in
14 various MCS, whether they are stable, such as ER-mitochondria contacts, or more labile and short-
15 lived, such as ER-TGN contact sites²⁷. The truncation of the MSP domain was shown to impair both
16 contact sites as reflected by altered mitochondrial shape and TGN protein turnover. With regard
17 to mitochondria, we also observed that VAPB is recruited to these contact sites. This may be
18 because more FFAT proteins are available as mitochondrial binding partners due to lack of
19 functional VAPA. VAPB, however, may not be able to promote cardiolipin-dependent
20 mitochondrial fusion in a similar manner as VAPA,²⁷ again arguing for a broader functional
21 repertoire of VAPA compared to VAPB. With regard to the TGN, we observed increased
22 recruitment of the cholesterol/PI4P exchanger OSBP ([Figures 4G and 4H](#)). Previously, we could
23 show that knocking-out VAPA shifts OSBP from the cytosol to the TGN²⁷, indicating a higher PI4P
24 level at the TGN resulting from decreased OSBP activity. Therefore, increased OSBP levels reflect
25 impaired VAPA-dependent MCS with the ER. Similarly, increased CERT levels were observed at
26 the TGN, as this protein also interacts with PI4P via its PH domain and with VAPA via its FFAT
27 motif. As both the mitochondrial and TGN phenotypes could not be rescued by VAPA Δ 78 in the

VAPA KO cells, we altogether provide strong support that the p.(Glu12*) mutation leads to disturbed contact sites.

An important question that followed was how impaired VAPA-dependent MCSs can lead to specific tissue defects in the patient, particularly in the lung. Surfactant production involves the formation and transport of a lipoprotein-like particle from the ER via the Golgi to the LB³⁶, which is a lysosome-related organelle^{37,38}. The LB is then filled with lipids due to the activity of phospholipid transporters such as ABCA3, allowing for further loading of the lipoprotein particle. A very intriguing hypothesis was therefore that ABCA3 can interact with VAPA to promote lipid transfer from the ER directly into LBs. Indeed, we found that ABCA3 itself contains a FFAT-like motif that permits interaction with VAPA (Figure 5E). Through this mechanism, this protein pair acts as a bridge facilitating the formation of functional ER-LB MCS, thereby enabling the accumulation of lipids in LBs (Figures 5G and 5H). Therefore, we postulate that non-vesicular lipid transfer proteins at the ER/LB interface may specifically deliver key lipids such as dipalmitoyl-PC or cholesterol to LBs for surfactant biogenesis. This may also explain the high expression levels of VAPA in AT2 cells^{39,40}.

Besides such impaired lipid transfer to the LBs from VAPA dysfunction, the patient's lavage lipidomics revealed elevated CE levels, and lung histology showed cholesterol clefts (Figures 1E and S1D). Similar cholesterol granulomas with crystal/cleft-like structures are characteristic for endogenous lipoid pneumonia often combined with PAP^{41,42}. X-ray diffraction identified these crystals as CE (cholesteryl palmitate and/or stearate), but not FC⁴¹. CE crystals are thought to originate from surfactant components not removed from the alveolar space by AT2 cells, which recycle about 90% of secreted surfactant^{43,44}, or from alveolar macrophages. In the present study, we could show that the reduced amount of FC in LBs of VAPA KO or p.(Glu12*) cells due to inefficient FC transport may lead to increased esterification and LD formation in the ER. Damage of AT2 cells due to VAPA dysfunction could eventually release cholesterol-rich membranes and organelles, while impaired recycling by AT2 cells and clearance by macrophages

could further contribute to the CE accumulation and surfactant defect. It may even be possible that VAPA dysfunction in the macrophages affects lipid transfer during the phagocytic process.

Another severe phenotype in the patient was retinal blindness. Given that mutations in a peroxisomal VAP binding partner, ACBD5, cause retinal dystrophy⁴⁵, this suggests that a disruption of ER-peroxisome tethering, and associated very-long-chain fatty acid metabolism dysfunction, may also underlie this phenotype in the patient. Moreover, for the patient's atopic dermatitis a possible explanation may be a decreased LB maturation in the epidermal keratinocytes.

A major limitation of the study is that so far only one patient with VAPA deficiency could be identified. However, it can also be expected that this report will increase the awareness for patients with similar phenotypes and, thus, additional pathogenic *VAPA* variants can be found in the future. Regardless of this ongoing search, this unique case has not only stimulated the functional validation of the VAPA p.(Glu12*) variant but also provided new insights into alveolar biology, in particular LB formation and surfactant production.

Acknowledgements

We thank B. Antonny, A. Patel (IPMC, Valbonne), for in-depth discussions and valuable comments.

We thank N. Leroudier and F. Brau (IPMC, Valbonne) for technical assistance and the IPMC Imaging and Cytometry facility, part of the MICA platform (GIS IBiSA). We also thank the ZMBH Imaging facility at Heidelberg University for providing support and access to microscopes.

This work was supported by the CNRS, Inserm, and the Agence Nationale de la Recherche (ANR-21-CE13-0021 (FLEXLINK) and ANR-25-CE13-5102 (VAPA-SURF)). We further acknowledge the European Research Council (ERC) under the European Horizon 2020 research and innovation

programme (Grant agreement No. 865408 (RENOPROTECT) to M.S), European Union's Seventh Framework Programme FP7 (chILD-EU, 305653 to M.G) and the Deutsche Forschungsgemeinschaft (DFG SI1303/5-1 (Heisenberg-Programm), DFG SI1303/7-1 to MS; DFG Gr970/9-2 to M.G). This work was granted access to the HPC resources of IDRIS under the allocation 2025-A0170714646 made by GENCI. A doctoral fellowship to Z. Grimanelli was provided by Polytech Nice Sophia (Université Côte d'Azur).

Author contributions

M.S. and B.M. conceived the study. M.S., B.M., Z.G., S.D., F.M., L.H. and J.A designed experiments. Z.G., S.D., F.M., L.H., and J.A. performed experiments. S.A. performed Tau-STED imaging. A.R.D.A., F.M.V. and D.H. performed lipidomics and mass spectrometry measurements. C.P. performed DNA cloning and protein purification. R.G. supervised and provided advice on molecular dynamics simulations. F.M., Ö.A-T., O.B., M.H., D.H., S.H. and M.G. provided sequencing and clinical data from the patient. B.M. and M.S. wrote and edited the manuscript. All the authors reviewed the manuscript.

Declaration of interests

The authors declare no competing interests.

Inclusion and diversity

We support inclusive, diverse and equitable conduct of research.

STAR★Methods

KEY RESOURCES TABLE

REAGENT or RESOURCE	SOURCE	ID
Antibodies		
Rabbit anti OSBP	Atlas Antibodies	Cat# HPA039227
Rabbit anti CERT	Proteintech	Cat# 15191-1-AP
Rabbit anti VAPA	Atlas Antibodies	Cat# HPA009174

Rabbit anti VAPA	Proteintech	Cat# 15275-1-AP
Rabbit anti VAPB	Atlas Antibodies	Cat# HPA013144
Rabbit anti Tubulin- α	Sigma-Aldrich	Cat# Sab4500087
Mouse anti Flag	Sigma-Aldrich	Cat# F3165
Sheep anti TGN46	Biorad	Cat# AHP500G
Secondary Alexa Fluor-conjugated	Thermo Fisher Scientific	Cat# A32723
HRP-conjugated secondary	Jackson ImmunoResearch Labs	Cat# 111-035-047
Bacterial strains		
<i>Escherichia coli</i> BL21 (DE3)	IPMC resources	N/A
XL10-gold ultracompetent cells	Agilent technologies	Cat#200315
Chemicals, Peptides and Recombinant Proteins		
Jenelia Fluor 646 HaloTag-Ligand	Promega	Cat# GA112A
Filipin	Sigma-Aldrich	Cat# F9765
Sypro™ Orange protein gel stain	Invitrogen	Cat# S6650
MitoTracker-Red CMX Ros	Invitrogen	Cat# M7512
MitoTracker-Deep Red FM	Invitrogen	Cat# M22426
β -BODIPY™ FL C ₁₂ -HPC	Invitrogen	Cat# D3792
FFAT peptide	Proteogenix (Oberhausbergen, France)	N/A
Egg PC	Avanti Polar Lipids	Cat# 840051C
Brain PS	Avanti Polar Lipids	Cat# 840032C
Brain PI(4)P	Avanti Polar Lipids	Cat# 840045X
Liver PE	Avanti Polar Lipids	Cat# 840026C
Liver PI	Avanti Polar Lipids	Cat# 840042C
Rhodamine-PE	Avanti Polar Lipids	Cat# 810158C
SuperSignal West Femto Maximum Sensitivity	Thermo Scientific™	Cat# 34095
SuperSignal West Dura Extended Duration	Thermo Scientific™	Cat# 34076
HisPur™ Cobalt Resin	Thermo Scientific™	Cat# 89965
Amido black 10 B	Roth	Cat# 9590.1
Critical commercial assays		
Amaya Cell Line Nucleofector Kit V	Lonza	Cat# VCA-1003
jetOPTIMUS DNA transfection reagent	Polyplus	Cat# 101000025
PENTR™/D-TOPO™ Cloning kit	Thermo Scientific™	Cat# K240020SP
Gateway™ LR Clonase™ II ENzyme-Mix	Invitrogen	Cat# 11791020
QuickChange II Site-directed mutagenesis kit	Agilent technologies	Cat#200523
Experimental models: Cell lines		
hTERT-RPE1	ATCC	Cat# CRL-4000
A549	ATCC	Cat# CCL-185
Recombinant DNA		
pET21b-VAPA-WT-6His	(Subra et al., 2023)	N/A
pET21b -VAPA [79-230]-6His	This study	N/A
pEGFP-C1-VAPA-WT	F. Alpy	N/A
pEGFP-C1-VAPA-[79-249]	This study	N/A
pHTN-VAP-A-WT	(Subra et al., 2023)	N/A
pHTN-VAPA-[79-249]	This study	N/A
pET16b-StreptII.TEV.OSBP N-PH-FFAT (1-408)	(Jamenca et al., 2019)	N/A
pmCherry-N1-ABCA3 WT	This study	N/A
pmCherry-N1-ABCA3 Y524A/F525A	This study	N/A
pmCherry-N1-ABCA3 E690K	This study	N/A
2xFlag-C-pVAPACtrl	This study	N/A
2xFlag-C-pVAPA-Glu12*	This study	N/A
2xFlag-C-pVAPA-Glu12* M79G	This study	N/A
2xFlag-C-pVAPA-Glu12* M96G	This study	N/A
2xFlag-C-pVAPA-Glu12* M109G	This study	N/A
pCMV6-Entry-VAPA	OriGene Technologies Inc	Cat# RC201164
2xFlag-pDEST-C	Addgene	Cat# 118372
Software and algorithms		
MUSCLE	EMB-EBI	N/A
WebLogo 3	https://weblogo.threeplusone.com	N/A
Fiji	NIH, USA	N/A
OMERO	U Dundee & Open Microscopy Environment	N/A
Metamorph	Molecular Devices LLC	N/A
GraphPad Prism 10	GraphPad Software	N/A
Canvas X Draw	ACD system	N/A
Huygens Remote Manager version 3.7	Scientific Volume Imaging	CMLE algorithm
CellProfiler	Broad Institute	N/A
LAS X software 3.5.6.21594	Leica Microsystems	N/A
Lasergene 17	DNASTAR, Inc.	N/A

PyMOL 2.0	Schrödinger, LLC.	N/A
AlphaFold2	AlphaFold2.ipynb - Colab	N/A
GROMACS 2023.4	Gromacs.org	N/A
CHARMM36	https://academiccharmm.org/	N/A
VMD	http://www.ks.uiuc.edu/Research/vmd/	N/A
Python3	Python.org	N/A

RESOURCE AVAILABILITY

Lead contact

Further information and requests for resources and reagents should be directed to and will be fulfilled by the lead contact, Matias Simons (Matias.Simons@med.uni-heidelberg.de).

Materials availability

Plasmids generated in this study will be made available through requests to the lead contact.

Data and code availability

- Data including all raw image files reported in this paper will be shared by the lead contact upon request.

- This paper does not report original code.

- Any additional information required to reanalyze the data reported in this work paper is available from the lead contact upon request.

EXPERIMENTAL MODEL AND SUBJECT DETAILS

DNA sequencing

Informed consent for genetic testing and research was obtained from the family after counseling in accordance with national ethical standards and laws. The family underwent trio-exome sequencing according to local protocols. Segregation was assessed by Sanger sequencing. As no possibly causative variants were identified in known disease-associated genes and other

candidate genes explaining the individuals' phenotypes, the datasets were further evaluated in a research context. Variant prioritization was based on allele frequency and predicted functional impact using multiple *in silico* tools. Other rare variants were detected but excluded due to predicted benign impact or incompatibility with the observed phenotype.

Cell culture

Primary fibroblasts were derived from skin biopsies of the patient with VAPA c.34G>T; p.Glu12* variant after informed written consent was obtained from the family. Control cells were from an age and gender-matched healthy patient. Primary fibroblasts were cultured in DMEM (1X) with GlutaMAX™-I, supplemented with 10% FBS, 1% Pen/Strep and 1% Amphotericin B. Cells were cultured at 37°C, 5% CO₂ and high humidity in a CO₂ cell culture incubator.

Human immortalized retinal pigmented epithelial cells (hTERT-RPE1, ATCC Cat# CRL-4000; hereafter RPE1) were used as cellular model. RPE1 are genetically stable, lack transformed phenotypes, and are commonly used to study intracellular membrane traffic and dynamics. Human lung adenocarcinoma epithelial cells (A549, ATCC Cat# CCL-185; hereafter A549) were also used as cellular model. A549 cells are widely used as a model for alveolar type II epithelial cells, and serve as a reference line in studies of lung physiology. Both RPE1 and A549 cell lines were cultured in DMEM/F12 medium with GlutaMAX™ (Gibco) supplemented with 10% fetal calf serum (FCS) and 1% antibiotics (Zell Shield) at 37°C in a 5% CO₂ humidified atmosphere.

METHOD DETAILS

Plasmids

The 2xFlag-C-pVAPA-Glu12* and 2xFlag-C-pVAPACtrl plasmids were generated by gateway cloning. For the BP reaction the Thermo Scientific™ PENTR™/D-TOPO™ Cloning Kit was used to the manufacturer's instructions, using the provided entry vector pENTR™/D-TOPO®. The blunt end PCR products were produced using the primers listed in Table in S1. The primers were

designed so that the resulting PCR product contains a GGC codon (coding for Gly) instead of a stop codon, to fuse the ORF of the insert with the C-terminal 2xFlag tag of the destination vector. For 2xFlag-C-pVAPA-Glu12*, cDNA derived from VAPA-Glu12* fibroblasts was used as template DNA. For 2xFlag-C-pVAPACtrl, pCMV6-VAPA was used as template DNA. The resulting entry vectors were transformed in One Shot™ TOP10 Chemically Competent *E. coli*, using the manufacturer's heat shock transformation protocol. For the LR reaction the Gateway™ LR Clonase™ II Enzyme Mix was used according to the manufacturer's instruction, using the previously derived entry vectors and 2xFlag-pDEST-C as a destination vector. The resulting reaction mixture was transformed in One Shot™ TOP10 Chemically Competent *E. coli*, using the manufacturer's heat shock transformation protocol, to retrieve expression clones. The insert DNA sequence of entry vectors and expression clones was verified by Sanger sequencing. Single amino acid changes (M79G, M96G and M109G) were introduced to 2xFlag-C-pVAPA-Glu12* using the QuikChange II Site-Directed Mutagenesis Kit according to the manufacturer's instructions, using the primers indicated in Table S1. To obtain VAPA constructs missing residues 1-78, mutagenesis was performed from the three starting vectors pEGFP-C1 VAPA (FL; 1-249), pHTN VAPA (FL; 1-249) and pET21b+ VAPA His6 (8-230) previously described²⁷, by PCR amplification and restriction enzyme cloning method. Full-length human ABCA3, ABCA3 Y524A/F525A and ABCA3 E690K cDNA were obtained from Twist Biosciences and subcloned into pmCherry-N1 by the restriction enzyme cloning method.

Cell transfection

RPE1 and A549 cells were transfected using the Amaxa Nucleofector device (Lonza; X-01 program), Solution V (Lonza) and 2 µg of plasmids, for 24-48 h. For microscopy, cells were seeded in ibiTreat µ-Slides 8 Well or µ-Dish 35 mm (Ibidi) at suitable density to reach 50-90% confluence on the day of imaging. For Figure S2E and S2C, RPE1 cells were transfected using the jetOPTIMUS® DNA Transfection Reagent according to the manufacturer's instructions. Cells were seeded on 10 cm dishes and at suitable confluency, the transfections were performed using 10 µg

of plasmid, and 10 μ l of jetOPTIMUS® reagent. The cells were collected to prepare western blot samples 24 h post transfection.

Cell staining and imaging

For immunofluorescence, cells cultured on μ -slides (Ibidi) were washed once with PBS then fixed with paraformaldehyde (PFA) 4% and glutaraldehyde 0.1 % in PBS for 10 min. Fixed cells were soaked in PBS supplemented with NH₄Cl (50 mM) for 10 min, and then permeabilized in permeabilization buffer (Saponin 0.05 %, BSA 0.2 %, PBS) during 45 min at room temperature (RT). Cells were then immuno-labeled with primary antibodies (rabbit anti-OSBP or CERT (Atlas Antibodies), sheep anti-TGN46 (Biorad), diluted in permeabilization buffer) for 2 h at RT, washed 3 times with permeabilization buffer, further incubated with secondary Alexa Fluor-conjugated antibodies (Invitrogen; diluted in permeabilization buffer) and Hoechst for nuclear staining for 30 min at RT, and rinsed. Mitotracker Red (Invitrogen) staining was performed at 100 nM on living cells in growth medium during 30 min at 37°C, and then washed twice. For lipid droplet staining, cells were incubated with fresh media containing 2 μ M BODIPY 493/503 (Invitrogen) for 15 min at 37°C, washed with PBS and fixed with PFA 4% for 10 min at RT. Cells were subsequently washed three times with PBS before imaging. Bodipy staining intensity was calculated as area fraction per cell using ImageJ software. For filipin assays, A549 cells cultured on 35-mm μ -dishes (Ibidi) were fixed with paraformaldehyde (1.5%) for 20 min at RT, then stained with filipin (Sigma Aldrich) at 50 μ g/mL in PBS for 45 min at RT in the dark. Thereafter, cells were washed three times with PBS before imaging. For BODIPY-PC uptake into LBs, A549 cells cultured on 35-mm μ -dishes (Ibidi) were labelled with 1 μ g/mL BODIPY FL C12-HPC (Invitrogen) in growth medium for 30 min at 37°C. Then, cells were washed with warm PBS and chased for 16 h in fresh medium before imaging. Confocal images were acquired using a Zeiss LSM 780 (Carl Zeiss Microscopy, Jena) equipped with a multiline argon laser and diode lasers. All images were acquired through a 63x/1.4 NA Oil immersion objective using the ZEN software (Carl Zeiss Microscopy). Widefield

imaging was performed using a IX83 inverted microscope (Olympus) equipped with an iXon3 EMCCD camera (Andor) and an UPlanSApo 60X/1.35 Oil objective (Olympus).

Western Blotting

For western blotting, cells were seeded in 10 cm dishes. For sample collection, cells were washed with PBS and then scraped in 1 mL PBS. Thereafter, cells were centrifuged at 4°C, 1500 x g, for 5 min and resuspended in lysis buffer (0.1% SDS, 1% Triton® X-100 in PBS), before being sonicated for 2 seconds 5 times. Proteins were solubilized by rotating the samples for 1 hour at 4 °C. Afterwards, the samples were centrifuged at 4 °C, 14 000 x g, for 5 min and the supernatant was transferred to a new 1.5 mL microcentrifuge tube. Protein concentration of each sample was determined using AmidoBlack. The samples were adjusted to a common concentration (15-30 µg) in Laemmli buffer, boiled for 5 min at 95°C and applied to a SDS-PAGE. Gel blotting was performed on PVDF membrane using standard wet-blotting procedures. Membranes were blocked for 1 h in PBS + 0.1 % Tween-20 (PBST) supplemented with 5% skim milk and incubated in primary antibody overnight at 4 °C. Then, membranes were washed with PBST 3 times for 5-10 min each, incubated with a HRP secondary antibody for 1 h at RT, washed again 3 times for 5-10 min in PBST, followed by another 5-10 min wash with PBS. For blot imaging, SuperSignal™ West Femto Maximum Sensitivity or SuperSignal™ West Dura Extended Duration substrate was used, according to the manufacturer's instructions. A INTAS ECL Chemostar Imager was used to develop the blots.

qPCR

For RNA extraction, the Macherey-Nagel Nucleospin RNA Mini kit was used, according to the manufacturer's instructions. The RNA concentration of each sample was measured using a DeNovix DS-11 FX µVolume Spectrophotometer. The qScript cDNA Synthesis Kit was used, according to the manufacturer's instructions, to make cDNA. For the qPCR reaction, qPCRBIO SyGreen Mix was used according to the manufacturer's instructions. The samples were diluted to

1 contain 1 ng/μL cDNA and added to a 96 well plate, each reaction was run in triplicates. The
2 primers used are listed in Table S1. The qPCR was run using a QuantStudio 3 RT PCR System.

4 **Primary fibroblast lipidomics**

5 Lipidomics analysis was performed as described⁴⁶. The HPLC system consisted of an Ultimate
6 3000 binary HPLC pump, a vacuum degasser, a column temperature controller, and an auto
7 sampler (Thermo Scientific, Waltham, MA, USA). The column temperature was maintained at
8 25°C. The lipid extract was injected onto a "normal phase column" LiChrospher 2x250-mm silica-
9 60 column, 5 μm particle diameter (Merck, Darmstadt, Germany) and a "reverse phase
10 column" Acquity UPLC HSS T3, 1.8 μm particle diameter (Waters, Milford Massachusetts, USA). A
11 Q Exactive Plus Orbitrap (Thermo Scientific) mass spectrometer was used in the negative and
12 positive electrospray ionization mode. In both ionization modes, mass spectra of the lipid species
13 were obtained by continuous scanning from m/z 150 to m/z 2000 with a resolution of 280,000
14 full width at half maximum (FWHM).

15 An in-house developed pipeline, written in the R programming language, was used for data
16 processing. The RAW data files were converted to mzXML using MSconvert
17 (<https://doi.org/10.1038/nbt.2377>) in centroided mode. Peak finding and peak group finding
18 was done using the R package XCMS, with minor modifications to some functions for a better
19 representation of the Q Exactive data. Annotation of the peaks was done based on an in-house
20 database containing all possible (phospho)lipid species. Each combination of column (normal
21 phase or reverse phase) and scan mode (positive or negative) was processed separately; after
22 normalization, separate peak group lists were combined into two resulting lists, which were used
23 for statistical analysis.

24 Identification is based on exact mass (with 3 ppm tolerance) and retention time including
25 the relation between these two parameters, taking into account the different molecular species of
26 the lipid class⁴⁶.

1 **BAL lipidomics**

2 For quantitative lipidomics, internal standards were added prior to lipid extraction. A
3 volume of 50 to 150µl BAL was subjected to lipid extraction. The analysis of lipids was performed
4 by direct flow injection analysis (FIA) using a triple quadrupole mass spectrometer (FIA-MS/MS)
5 and a high-resolution hybrid quadrupole-Orbitrap mass spectrometer (FIA-FTMS). FIA-MS/MS
6 was performed in positive ion mode using the analytical setup and strategy described previously⁴⁷
7 . A fragment ion of m/z 184 was used for lysophosphatidylcholines (LPC). The following neutral
8 losses were applied: Phosphatidylethanolamine (PE) and lysophosphatidylethanolamine (LPE)
9 141, phosphatidylserine (PS) 185, phosphatidylglycerol (PG) 189 and phosphatidylinositol (PI)
10 277. Sphingosine-based ceramides (Cer) and hexosylceramides (Hex-Cer) were analyzed using a
11 fragment ion of m/z 264. PE-based plasmalogens (PE P) were analyzed according to the principles
12 described by Zemski-Berry⁴⁸. Glycerophospholipid species annotation was based on the
13 assumption of even numbered carbon chains only. A detailed description of the FIA-FTMS method
14 was published recently⁴⁹. Triglycerides (TG), diglyceric+ at a target resolution of 140,000 (at 200
15 m/z). CE species were corrected for their species-specific response. Phosphatidylcholines (PC),
16 PC ether (PC O) and sphingomyelins (SM) were analyzed in negative ion mode m/z 520-960 as
17 $[M+HCOO]^-$ at the same resolution setting. Analysis of free cholesterol (FC) was performed by
18 multiplexed acquisition (MSX) of the $[M+NH_4]^+$ of FC and the deuterated internal standard
19 (FC[D7]).

20

21 **Histology**

22 Lung biopsies were fixed in 10% buffered formalin and paraffin embedded. 2-3µm slides were cut
23 and stained with Hematoxylin-Eosin, PAS, Elastica-van-Giesson and Prussian-blue according to
24 standard procedures. Slides were evaluated using a Olympus microscope (BX53, Olympus, Japan).

25

26 **Transmission electron microscopy**

1 Lung biopsies were fixed in 1.5% PFA, 1.5% glutaraldehyde in 0.15 M Hepes buffer. The samples
2 were then embedded in epoxy resin according to a standard protocol which involved subsequent
3 incubation with 1% osmium tetroxide, half-saturated uranyl acetate and an ascending acetone
4 series⁵⁰. From the embedded samples ultrathin sections of 60-80 nm thickness were generated
5 and poststained with uranyl acetate and lead citrate. The sections were analysed using a
6 transmission electron microscope (Morgagni, FEI, Eindhoven, the Netherlands).

8 **Tau-stimulated emission depletion (STED) microscopy**

9 Cells were transfected with pHTN HaloTag plasmids using the Amaxa Nucleofector device (Lonza),
10 and plated in μ -Slides 8 Well glass coverslip bottom (Ibidi). 24 h after transfection, cells were
11 labelled with 0.2 mM Janelia Fluor 646 HaloTag-Ligand (Promega) in growth medium for 30 min
12 at 37°C. Cells were then washed twice to remove unbound dye and further incubated for 30 min
13 at 37°C in growth medium. Finally, cells were washed in PBS, fixed with PFA 4%/glutaraldehyde
14 0.1% and washed again in PBS before imaging. Tau-STED imaging was performed on a Leica TCS
15 SP8 STED 3X system (Leica Microsystems) equipped with a pulsed white-light laser for excitation
16 and a 775 nm pulsed depletion laser configured for hybrid-gated Tau-STED acquisition. Images
17 were acquired through a 100x/1.4 NA Oil objective controlled with LAS X software (Leica
18 Microsystems). Janelia Fluor 646 was excited at 633 nm and Tau-STED detection was performed
19 using the falcon module of the software. Images have a 15 nm pixel size.

21 **MD simulations**

22 The MSP domain of human VAPA WT (res. 1-128) bound to the human OSBP FFAT motif region
23 (res. 346-379) was retrieved from the NMR structure of the complex (PDB : 2RR3)²⁶. The VAPA
24 MSP Δ 78 was built with the AlphaFold2 tool^{51,52}. Their electrostatic surface was obtained with
25 PyMOL 2.0 software. MD simulations of the MSP domains alone, or bound to the FFAT motif, were
26 performed with GROMACS 2023.4. For the MSP Δ 78–FFAT complex, the structure was generated
27 by aligning MSP Δ 78 onto the WT MSP from the NMR complex. The protein's topology was

obtained with the CHARMM36 force-field^{53,54}, adding COO⁻ and NH₃⁺ at the termini. The proteins were centered in a cubic box, at a minimum distance of 2 nm from box edges. Solvent molecules were added with the TIP3P water model configuration. Na and Cl ions were added to neutralize the simulation box, at a concentration of 120 mM. Energy minimization was performed using the steepest descent minimization algorithm for the subsequent 50,000 steps with a step size of 0.01 nm. A cutoff distance of 1.2 nm was used for generating the neighbor list, updated at every step. Long-range electrostatic interactions were calculated using the particle mesh Ewald summation methods. Periodic boundary conditions and flexible water were used. A 200 ps NVT equilibration was performed, with a 2 ps time-step. During equilibration, the protein was restrained. All bonds were constrained by the LINear Constraints Solver (LINCS) constraint algorithm. A 200 ps NPT equilibration was performed similar to the NVT equilibration. During the production run, the V-rescale thermostat and Parrinello–Rahman barostat stabilized the temperature at 310.15 K and pressure at 1 bar, respectively. The simulations were performed for 500 ns for the systems with MSP domains alone, and 1 μ s for MSP-FFAT systems, with a time-step of 2 fs, with the two coupling groups Protein and Water-Ions. MD analyses of the root-mean-square deviation (RMSD) on C α , binding energies and MSP-FFAT contacts < 4 Å were performed using GROMACS utilities. The occurrence of hydrogen bonds (H-bonds) during the three replicates of each system were calculated with the H-Bonds tool of the VMD software. Hydrogen bonds were defined with a maximal distance of 3.5 Å and a 30° angle. Python scripts were written to obtain the figures. Movies and images have been generated with VMD and PyMOL 2.0 software, respectively.

Protein expression and purification

OSBP N-PH-FFAT (res. 1-408), VAPA-His and VAPA Δ 78-His constructs, sub-cloned into pET-21b, were expressed in *E. coli* BL21 (DE3) and purified as previously described²⁷. N-PH-FFAT had a N-ter 6xHis tag-StrepII-TEV site, VAPA-His constructs had a C-terl 6xHis-tag replacing protein transmembrane region. After protein expression, bacteria were lysed in a cell disruptor at 1600 psi and incubated for 30 min on ice with DNase and MgCl₂ (5mM) before ultracentrifugation

(125,000 x g). Proteins were purified using HisPur™ Cobalt Resin (Thermo Scientific). For N-PH-FFAT, protein fractions were pooled and cleaved with TEV protease overnight at 4°C. Digested proteins were purified on SourceQ HR 10/10 column (GE Healthcare) with a 0-1 M NaCl gradient in 25 mM Tris pH7.5 followed by a Sephacryl S200 HK16/70 column (GE Healthcare) equilibrated in 25 mM Tris pH7.5, 120 mM NaCl, 2 mM DTT, using an AKTA purifier system (GE Healthcare). For VAPA-His constructs, eluted protein fractions were pooled, concentrated and further purified on a Sephacryl S200 HR/XK 16/70 column (GE Healthcare) equilibrated in 25 mM Tris pH 7.5, 120 mM NaCl, 1 mM DTT.

Liposome preparation and flotation assay

egg PC, brain PS, liver PE, Rhodamine-PE and brain PI(4)P lipids (62/5/17/2/4 mol%) were mixed in chloroform/methanol (2:1), and the solvent was removed in a rotary evaporator. The lipid film was hydrated in 50 mM HEPES pH 7.4, 120 mM K acetate (HK buffer, which was degassed before use) to reach a concentration of 2 mM. The suspension was then frozen in liquid nitrogen and thawed in a water bath (37°C) five times. Liposomes were extruded through 0.1 mm pore size polycarbonate filters using hand extruder (Avanti Polar Lipids) and were used within 1-2 days. For the flotation assay, liposomes (1 mM) and N-PH-FFAT (1 μM) were incubated for 5 min in HK buffer supplemented with 1 mM MgCl₂ (HKM buffer) at RT in a Beckman polycarbonate centrifuge tube. 1 μM of VAPA His or VAPAΔ78-His was added with or without preincubation with FFAT peptide 5 min at RT (WCSGKGDMSEDDENEFFDAPEIITMPENLGH, Proteogenix). The 150 μL mixture was incubated 10 min at 37°C under agitation and mixed with HK buffer supplemented with 60% sucrose (100 μL) and then overlaid with an intermediate sucrose solution made of HK buffer with 24% sucrose (200 μL) and a layer (50 μL) of HKM buffer. After centrifugation at 55,000 rpm in a TLS 55 (Beckman) swing rotor for 90 min at 25°C, three fractions (bottom, medium, and top) of 250, 150 and 100 μL were collected and analyzed by SDS-PAGE using Sypro-Orange staining.

QUANTIFICATION AND STATISTICAL ANALYSIS

Quantification of lamellar bodies from EM images of lung samples

To obtain quantitative data, images of alveolar epithelial type II (AT2) cells were obtained by systematic uniform random sampling. AT2 cells were then classified whether they contained LBs with normal or with abnormal appearance. Afterwards, the images were classified into three categories: 1. mostly normal LBs, 2. moderate LB alterations 3. severe LB alterations. In each subset of the cells the volume fraction of LB dense cores was estimated by point counting. As control lungs, we used archived human lung samples from the Institute of Anatomy at the University of Bern⁵⁵ (under permission No. 2263-2014 of Hannover Medical School).

Quantification of fluorescence microscopy images

For lipid enrichment (BODIPY-PC or filipin signal) at LBs, a LB mask using the ABCA3-mCherry signal was applied on the green or blue channel using Fiji (ImageJ, NIH), and a ratio between the average fluorescence in these regions and the average fluorescence of the entire cell was determined. For TGN/cytosol ratios of OSBP, two regions of interest (ROIs) of the same area were drawn in the TGN and in the cytosol. The average fluorescence was determined for each ROI and the ratio was then calculated. In all superplots illustrating image quantification, each point represents one cell analyzed, and each experiment was performed 3 times independently. Colocalization measurements (Pearson test) were performed using the MeasureColocalization module from CellProfiler (Broad Institute) on images where the background was first subtracted. Statistical analyzes were done in PRISM : * $p < 0.1$, ** $p < 0.01$, *** $p < 0.001$, **** $p < 0.0001$.

Mitochondria form factor

To quantify mitochondria morphology, images were processed automatically through a custom pipeline in CellProfiler. Mitochondria and transfected cells were first accentuated and binarized using the EnhanceOrSuppressFeatures module. Thereafter, mitochondria objects were identified using the IdentifyPrimaryObject module, and linked to transfected or not transfected cells with

the MaskObjects module. Finally, the MeasureObjectSizeShape module enabled measuring objects shape, notably according to the form factor ($4\pi \cdot \text{Area} / \text{Perimeter}^2$). As form factor values above 1 can arise from edge segmentation artifacts, we corrected this while retaining truly round mitochondria by applying a tolerance threshold of 1.3 and excluded higher values. Superplots illustrating image quantification were obtained with PRISM or python, each point represents one cell analyzed, and each experiment was performed 3 times independently.

References

1. Reinisch, K.M., Camilli, P.D., and Melia, T.J. (2025). Lipid Dynamics at Membrane Contact Sites. *Annu. Rev. Biochem.* 94, 479–502. <https://doi.org/10.1146/annurev-biochem-083024-122821>.
2. Voeltz, G.K., Sawyer, E.M., Hajnóczky, G., and Prinz, W.A. (2024). Making the connection: How membrane contact sites have changed our view of organelle biology. *Cell* 187, 257–270. <https://doi.org/10.1016/j.cell.2023.11.040>.
3. Balla, T., Kim, Y.J., Alvarez-Prats, A., and Pemberton, J. (2019). Lipid Dynamics at Contact Sites Between the Endoplasmic Reticulum and Other Organelles. *Annu. Rev. Cell Dev. Biol.* 35, 85–109. <https://doi.org/10.1146/annurev-cellbio-100818-125251>.
4. Khaddaj, R., and Kukulski, W. (2023). Piecing together the structural organisation of lipid exchange at membrane contact sites. *Curr. Opin. Cell Biol.* 83, 102212. <https://doi.org/10.1016/j.ceb.2023.102212>.
5. Wong, L.H., Gatta, A.T., and Levine, T.P. (2019). Lipid transfer proteins: the lipid commute via shuttles, bridges and tubes. *Nat Rev Mol Cell Bio* 20, 85–101. <https://doi.org/10.1038/s41580-018-0071-5>.
6. Levine, T.P. (2025). Update on VAP, a ubiquitous signpost for the ER. *Biol. Chem.* 0. <https://doi.org/10.1515/hsz-2025-0199>.
7. Kors, S., Costello, J.L., and Schrader, M. (2022). VAP Proteins – From Organelle Tethers to Pathogenic Host Interactors and Their Role in Neuronal Disease. *Frontiers Cell Dev Biology* 10, 895856. <https://doi.org/10.3389/fcell.2022.895856>.
8. Loewen, C.J.R., Roy, A., and Levine, T.P. (2003). A conserved ER targeting motif in three families of lipid binding proteins and in Opi1p binds VAP. *Embo J* 22, 2025–2035. <https://doi.org/10.1093/emboj/cdg201>.
9. Mattia, T.D., Martinet, A., Ikhlef, S., McEwen, A.G., Nominé, Y., Wendling, C., Poussin-Courmontagne, P., Voilquin, L., Eberling, P., Ruffenach, F., et al. (2020). FFAT motif phosphorylation controls formation and lipid transfer function of inter-organelle contacts. *Embo J*, e104369. <https://doi.org/10.15252/emboj.2019104369>.
10. Neefjes, J., and Cabukusta, B. (2021). What the VAP: The Expanded VAP Family of Proteins Interacting With FFAT and FFAT-Related Motifs for Interorganellar Contact. *Contact* 4, 251525642110122. <https://doi.org/10.1177/25152564211012246>.
11. Subra, M., Grimanelli, Z., Gautier, R., and Mesmin, B. (2023). Stranger Twins: A Tale of Resemblance and Contrast Between VAP Proteins. *Contact* 6, 25152564231183897. <https://doi.org/10.1177/25152564231183897>.
12. Murphy, S.E., and Levine, T.P. (2016). VAP, a Versatile Access Point for the Endoplasmic Reticulum: Review and analysis of FFAT-like motifs in the VAPome. *Biochimica Et Biophysica Acta Bba - Mol Cell Biology Lipids* 1861, 952–961. <https://doi.org/10.1016/j.bbalip.2016.02.009>.
13. Toro, N. del, Shrivastava, A., Ragueneau, E., Meldal, B., Combe, C., Barrera, E., Perfetto, L., How, K., Ratan, P., Shirodkar, G., et al. (2021). The IntAct database: efficient access to fine-grained

molecular interaction data. *Nucleic Acids Res.* 50, D648–D653.
<https://doi.org/10.1093/nar/gkab1006>.

14. Mesmin, B., Bigay, J., Moser von Filseck, J., Lacas-Gervais, S., Drin, G., and Antonny, B. (2013). A Four-Step Cycle Driven by PI(4)P Hydrolysis Directs Sterol/PI(4)P Exchange by the ER-Golgi Tether OSBP. *Cell* 155, 830–843. <https://doi.org/10.1016/j.cell.2013.09.056>.

15. Mesmin, B., Kovacs, D., and D'Angelo, G. (2019). Lipid exchange and signaling at ER–Golgi contact sites. *Curr Opin Cell Biol* 57, 8–15. <https://doi.org/10.1016/j.ceb.2018.10.002>.

16. Nishimura, A.L., Mitne-Neto, M., Silva, H.C.A., Richieri-Costa, A., Middleton, S., Cascio, D., Kok, F., Oliveira, J.R.M., Gillingwater, T., Webb, J., et al. (2004). A Mutation in the Vesicle-Trafficking Protein VAPB Causes Late-Onset Spinal Muscular Atrophy and Amyotrophic Lateral Sclerosis. *Am J Hum Genetics* 75, 822–831. <https://doi.org/10.1086/425287>.

17. Borgese, N., Navone, F., Nukina, N., and Yamanaka, T. (2021). Mutant VAPB: Culprit or Innocent Bystander of Amyotrophic Lateral Sclerosis? *Contact* 4, 25152564211022515. <https://doi.org/10.1177/25152564211022515>.

18. McCune, B.T., Tang, W., Lu, J., Eaglesham, J.B., Thorne, L., Mayer, A.E., Condiff, E., Nice, T.J., Goodfellow, I., Krezel, A.M., et al. (2017). Noroviruses Co-opt the Function of Host Proteins VAPA and VAPB for Replication via a Phenylalanine–Phenylalanine–Acidic–Tract–Motif Mimic in Nonstructural Viral Protein NS1/2. *Mbio* 8, e00668-17. <https://doi.org/10.1128/mbio.00668-17>.

19. Kabashi, E., Oussini, H.E., Bercier, V., Gros-Louis, F., Valdmanis, P.N., McDearmid, J., Meijer, I.A., Dion, P.A., Dupre, N., Hollinger, D., et al. (2013). Investigating the contribution of VAPB/ALS8 loss of function in amyotrophic lateral sclerosis. *Hum Mol Genet* 22, 2350–2360. <https://doi.org/10.1093/hmg/ddt080>.

20. Kotzot, D. (2001). Complex and segmental uniparental disomy (UPD): review and lessons from rare chromosomal complements. *J. Méd. Genet.* 38, 497. <https://doi.org/10.1136/jmg.38.8.497>.

21. Kotzot, D. (2008). Complex and segmental uniparental disomy updated. *J. Méd. Genet.* 45, 545. <https://doi.org/10.1136/jmg.2008.058016>.

22. Kurosaki, T., and Maquat, L.E. (2016). Nonsense-mediated mRNA decay in humans at a glance. *J. Cell Sci.* 129, 461–467. <https://doi.org/10.1242/jcs.181008>.

23. Ozisik, G., Mantovani, G., Achermann, J.C., Persani, L., Spada, A., Weiss, J., Beck-Peccoz, P., and Jameson, J.L. (2003). An Alternate Translation Initiation Site Circumvents an Amino-Terminal DAX1 Nonsense Mutation Leading to a Mild Form of X-Linked Adrenal Hypoplasia Congenita. *J. Clin. Endocrinol. Metab.* 88, 417–423. <https://doi.org/10.1210/jc.2002-021034>.

24. James, C., and Kehlenbach, R.H. (2021). The Interactome of the VAP Family of Proteins: An Overview. *Cells* 10, 1780. <https://doi.org/10.3390/cells10071780>.

25. Loewen, C.J.R., and Levine, T.P. (2005). A Highly Conserved Binding Site in Vesicle-associated Membrane Protein-associated Protein (VAP) for the FFAT Motif of Lipid-binding Proteins. *J Biol Chem* 280, 14097–14104. <https://doi.org/10.1074/jbc.m500147200>.

26. Furuita, K., Jee, J., Fukada, H., Mishima, M., and Kojima, C. (2010). Electrostatic Interaction between Oxysterol-binding Protein and VAMP-associated Protein A Revealed by NMR and Mutagenesis Studies. *J Biol Chem* 285, 12961–12970. <https://doi.org/10.1074/jbc.m109.082602>.

27. Subra, M., Dezi, M., Bigay, J., Lacas-Gervais, S., Cicco, A.D., Araújo, A.R.D., Abélanet, S., Fleuriot, L., Debayle, D., Gautier, R., et al. (2023). VAP-A intrinsically disordered regions enable versatile tethering at membrane contact sites. *Dev Cell* 58, 121–138.e9. <https://doi.org/10.1016/j.devcel.2022.12.010>.

28. Péresse, T., Kovacs, D., Subra, M., Bigay, J., Tsai, M.-C., Polidori, J., Gautier, R., Desrat, S., Fleuriot, L., Debayle, D., et al. (2020). Molecular and cellular dissection of the oxysterol-binding protein cycle through a fluorescent inhibitor. *J Biol Chem* 295, 4277–4288. <https://doi.org/10.1074/jbc.ra119.012012>.

29. Zarbock, R., Kaltenborn, E., Frixel, S., Wittmann, T., Liebisch, G., Schmitz, G., and Griesse, M. (2015). ABCA3 protects alveolar epithelial cells against free cholesterol induced cell death. *Biochim. Biophys. Acta (BBA) - Mol. Cell Biol. Lipids* 1851, 987–995. <https://doi.org/10.1016/j.bbalip.2015.03.004>.

30. Matsumura, Y., Ban, N., and Inagaki, N. (2008). Aberrant catalytic cycle and impaired lipid transport into intracellular vesicles in ABCA3 mutants associated with nonfatal pediatric

interstitial lung disease. *Am. J. Physiol.-Lung Cell. Mol. Physiol.* 295, L698–L707.
<https://doi.org/10.1152/ajplung.90352.2008>.

31. Slee, J.A., and Levine, T.P. (2019). Systematic Prediction of FFAT Motifs Across Eukaryote Proteomes Identifies Nucleolar and Eisosome Proteins With the Predicted Capacity to Form Bridges to the Endoplasmic Reticulum. *Contact* 2, 2515256419883136.
<https://doi.org/10.1177/2515256419883136>.

32. Buisson, M., Anczuków, O., Zetoune, A.B., Ware, M.D., and Mazoyer, S. (2006). The 185delAG mutation (c.68_69delAG) in the BRCA1 gene triggers translation reinitiation at a downstream AUG codon. *Hum. Mutat.* 27, 1024–1029. <https://doi.org/10.1002/humu.20384>.

33. Cohen, S., Kramarski, L., Levi, S., Deshe, N., David, O.B., and Arbely, E. (2019). Nonsense mutation-dependent reinitiation of translation in mammalian cells. *Nucleic Acids Res.* 47, 6330–6338. <https://doi.org/10.1093/nar/gkz319>.

34. Moey, C., Topper, S., Karn, M., Johnson, A.K., Das, S., Vidaurre, J., and Shoubridge, C. (2016). Reinitiation of mRNA translation in a patient with X-linked infantile spasms with a protein-truncating variant in ARX. *Eur. J. Hum. Genet.* 24, 681–689.
<https://doi.org/10.1038/ejhg.2015.176>.

35. Stump, M.R., Gong, Q., Packer, J.D., and Zhou, Z. (2012). Early LQT2 nonsense mutation generates N-terminally truncated hERG channels with altered gating properties by the reinitiation of translation. *J. Mol. Cell. Cardiol.* 53, 725–733. <https://doi.org/10.1016/j.yjmcc.2012.08.021>.

36. Sever, N., Miličić, G., Bodnar, N.O., Wu, X., and Rapoport, T.A. (2021). Mechanism of Lamellar Body Formation by Lung Surfactant Protein B. *Mol Cell* 81, 49–66.e8.
<https://doi.org/10.1016/j.molcel.2020.10.042>.

37. Dietl, P., and Frick, M. (2021). Channels and Transporters of the Pulmonary Lamellar Body in Health and Disease. *Cells* 11, 45. <https://doi.org/10.3390/cells11010045>.

38. Klein, S., Wimmer, B.H., Winter, S.L., Kolovou, A., Laketa, V., and Chlanda, P. (2021). Post-correlation on-lamella cryo-CLEM reveals the membrane architecture of lamellar bodies. *Commun Biology* 4, 137. <https://doi.org/10.1038/s42003-020-01567-z>.

39. Koenitzer, J.R., Wu, H., Atkinson, J.J., Brody, S.L., and Humphreys, B.D. (2020). Single-Nucleus RNA-Sequencing Profiling of Mouse Lung. Reduced Dissociation Bias and Improved Rare Cell-Type Detection Compared with Single-Cell RNA Sequencing. *Am. J. Respir. Cell Mol. Biol.* 63, 739–747. <https://doi.org/10.1165/rcmb.2020-0095ma>.

40. Karlsson, M., Zhang, C., Méar, L., Zhong, W., Digre, A., Katona, B., Sjöstedt, E., Butler, L., Odeberg, J., Dusart, P., et al. (2021). A single-cell type transcriptomics map of human tissues. *Sci. Adv.* 7, eabh2169. <https://doi.org/10.1126/sciadv.abh2169>.

41. Glancy, D.L., Frazier, P.D., and Roberts, W.C. (1968). Pulmonary parenchymal cholesterol-ester granulomas in patients with pulmonary hypertension. *Am. J. Med.* 45, 198–210.
[https://doi.org/10.1016/0002-9343\(68\)90038-7](https://doi.org/10.1016/0002-9343(68)90038-7).

42. Antoon, J.W., Hernandez, M.L., Roehrs, P.A., Noah, T.L., Leigh, M.W., and Byerley, J.S. (2016). Endogenous lipid pneumonia preceding diagnosis of pulmonary alveolar proteinosis. *Clin. Respir. J.* 10, 246–249. <https://doi.org/10.1111/crj.12197>.

43. Whitsett, J.A., Wert, S.E., and Weaver, T.E. (2010). Alveolar Surfactant Homeostasis and the Pathogenesis of Pulmonary Disease. *Annu. Rev. Med.* 61, 105–119.
<https://doi.org/10.1146/annurev.med.60.041807.123500>.

44. Young, S.L., Fram, E.K., Larson, E., and Wright, J.R. (1993). Recycling of surfactant lipid and apoprotein-A studied by electron microscopic autoradiography. *Am. J. Physiol.-Lung Cell. Mol. Physiol.* 265, L19–L26. <https://doi.org/10.1152/ajplung.1993.265.1.119>.

45. Dawes, M.L., Haberland, J.P., Islinger, M., and Schrader, M. (2025). The neurological pathology of peroxisomal ACBD5 deficiency – lessons from patients and mouse models. *Front. Mol. Neurosci.* 18, 1602343.
<https://doi.org/10.3389/fnmol.2025.1602343>.

46. Herzog, K., Pras-Raves, M.L., Vervaart, M.A.T., Luyf, A.C.M., Kampen, A.H.C. van, Wanders, R.J.A., Waterham, H.R., and Vaz, F.M. (2016). Lipidomic analysis of fibroblasts from Zellweger spectrum disorder patients identifies disease-specific phospholipid ratios[S]. *J. Lipid Res.* 57, 1447–1454.
<https://doi.org/10.1194/jlr.m067470>.

47. Liebisch, G., Lieser, B., Rathenberg, J., Drobnik, W., and Schmitz, G. (2004). High-throughput quantification of phosphatidylcholine and sphingomyelin by electrospray ionization tandem mass spectrometry coupled with isotope correction algorithm. *Biochim. Biophys. Acta (BBA) - Mol. Cell Biol. Lipids* 1686, 108–117. <https://doi.org/10.1016/j.bbalip.2004.09.003>.
48. Berry, K.A.Z., and Murphy, R.C. (2004). Electrospray ionization tandem mass spectrometry of glycerophosphoethanolamine plasmalogen phospholipids. *J. Am. Soc. Mass Spectrom.* 15, 1499–1508. <https://doi.org/10.1016/j.jasms.2004.07.009>.
49. Höring, M., Ejsing, C.S., Krautbauer, S., Ertl, V.M., Burkhardt, R., and Liebisch, G. (2021). Accurate quantification of lipid species affected by isobaric overlap in Fourier-transform mass spectrometry. *J. Lipid Res.* 62, 100050. <https://doi.org/10.1016/j.jlr.2021.100050>.
50. Mühlfeld, C., Rothen-Rutishauser, B., Vanhecke, D., Blank, F., Gehr, P., and Ochs, M. (2007). Visualization and quantitative analysis of nanoparticles in the respiratory tract by transmission electron microscopy. *Part. Fibre Toxicol.* 4, 11. <https://doi.org/10.1186/1743-8977-4-11>.
51. Jumper, J., Evans, R., Pritzel, A., Green, T., Figurnov, M., Ronneberger, O., Tunyasuvunakool, K., Bates, R., Žídek, A., Potapenko, A., et al. (2021). Highly accurate protein structure prediction with AlphaFold. *Nature* 596, 583–589. <https://doi.org/10.1038/s41586-021-03819-2>.
52. Mirdita, M., Schütze, K., Moriwaki, Y., Heo, L., Ovchinnikov, S., and Steinegger, M. (2022). ColabFold: making protein folding accessible to all. *Nat. Methods* 19, 679–682. <https://doi.org/10.1038/s41592-022-01488-1>.
53. Brooks, B.R., Brooks, C.L., Mackerell, A.D., Nilsson, L., Petrella, R.J., Roux, B., Won, Y., Archontis, G., Bartels, C., Boresch, S., et al. (2009). CHARMM: The biomolecular simulation program. *J. Comput. Chem.* 30, 1545–1614. <https://doi.org/10.1002/jcc.21287>.
54. Huang, J., and MacKerell, A.D. (2013). CHARMM36 all-atom additive protein force field: Validation based on comparison to NMR data. *J. Comput. Chem.* 34, 2135–2145. <https://doi.org/10.1002/jcc.23354>.
55. Gehr, P., Bachofen, M., and Weibel, E.R. (1978). The normal human lung: ultrastructure and morphometric estimation of diffusion capacity. *Respir. Physiol.* 32, 121–140. [https://doi.org/10.1016/0034-5687\(78\)90104-4](https://doi.org/10.1016/0034-5687(78)90104-4).

Figure legends

Figure 1: A homozygous nonsense variant in *VAPA* is associated with syndromic lung disease

A) Patient at 3.5 years.

B) Nail clubbing in fingers and toes.

C) First chest x-ray at age 3.7 years. Diffuse reticulation some, diffuse ground glass, right lower lobe (upper left). Chest CT (3 mm) age 3.8 y inter- and intralobular reticulation, ground glass opacification, crazy paving (lower left). CT (1 mm) age 5.4 y intralobular reticulation, diffuse lung cysts, traction bronchiectasis, pulmonary fibrosis (upper and lower right).

- D) Lung lavage lipidomics of the patient (red) compared to controls (black) and other PAP cases (autoimmune PAP, PAP due to *CSF2RA* variants; green).
- E) Post mortem patient lung tissue histology showing hypoplastic and cystically dilated airspaces filled with proteinaceous eosinophilic material with large numbers of cholesterol clefts and foam cells (top panels). Lymphoid hyperplasia with several small lymphoid aggregates (white arrow head) without germinal centres. Airspaces are lined by hyperplastic AT2 cells (bottom left, arrow head). Mild interstitial inflammatory infiltrate and interstitial fibrosis with increase in interstitial collagen (red in EvG-stain) (bottom panels). Intimal fibrosis partly with myxoid features in some pulmonary arteries (A) and veins (V).
- F) Transmission electron microscopy on the patient's lung tissue with quantification of normal and dysmorphic LB.
- G) Sequencing chromatograms showing the presence of the homozygous and heterozygous variant in the patient and mother, respectively. The variant is absent in the father.

Figure 2 : Alternative translation initiation sites drive expression of VAPA variant

- A) mRNA levels of VAPA and VAPB in the control and VAPA-Glu12* fibroblasts.
- B) Western blots for VAPA reveal bands of lower molecular weight in VAPA p.(Glu12*) cells. # and ## indicate two different primary anti-VAPA antibodies. VAPB protein levels are unchanged.
- C) Immunofluorescence stainings of VAPA and VAPB in control and VAPA-Glu12* fibroblasts. VAPB is recruited to ER subdomains in VAPA-Glu12* fibroblasts.
- D) Schematic diagram of alternative translation start codons that could possibly give rise to truncated variants of VAPA.
- E) Expression of VAPA-Glu12*-2xFLAG constructs with mutated alternative start codons, or no additional mutation (indicated by "-").

Figure 3 : VAPΔ78 MSP domain is predicted to be structurally unstable and exhibits poor FFAT binding

- A) Dynamic behavior of VAPA MSP WT (green lines) or Δ78 (blue lines) during 500 ns of MD simulation, represented by root-mean-square deviations (RMSD).
- B) Left, ribbon representation of VAPA MSP structure. Right, surface representation colored according to electrostatic potential.
- C) Same structural representations as those described in B using a conformation of MSPΔ78 obtained after 500 ns simulation.
- D) Interaction energy between MSP WT (green) or Δ78 (blue) and OSBP FFAT region. One point represents one simulation frame.
- E) Electrostatic and van der Waals contribution in the binding of the OSBP FFAT peptide to MSP WT or Δ78.
- F) and G) H-bond frequency between OSBP FFAT residues and MSP WT or Δ78 residues, expressed in percentage of simulation time.
- H) Number and stability of contacts (<4 Å) between MSP WT (green lines) or MSPΔ78 (blue lines) and FFAT over three simulations of 1 μs.
- I) Scheme of the flotation assay. OSBP N-PH-FFAT (res. 1-408) bound to PI(4)P liposomes was incubated with VAPA-His WT or Δ78 mutant constructs. The suspension was adjusted to 30% w/v sucrose and overlaid with two cushions of decreasing sucrose density. After ultracentrifugation, proteins bound to liposomes were retrieved on the top fraction.
- J) Top and bottom fractions analyzed by SDS-PAGE and Sypro-orange staining. When indicated a peptide encompassing the FFAT motif of OSBP was added as a competitor.
- K) Quantification of the fraction of VAPA-His bound to N-PH-FFAT. Data are means of 2 independent experiments .

Figure 4 : Patient fibroblasts exhibit cellular phenotypes resembling those of VAPA KO cells

1 A) Control and VAPA-Glu12* fibroblasts were fixed, permeabilized and processed for
2 immunofluorescence to assess the localization of OSBP and the TGN marked by TGN46 (anti-
3 OSBP and anti-TGN46 followed by staining with Alexa Fluor-conjugated secondary
4 antibodies, green and magenta, respectively), and imaged by confocal microscopy. Right,
5 Pearson's correlation coefficient between OSBP and TGN46. Measurements were performed
6 on 35-37 cells for each condition with the mean values indicated by the black lines.

7 B) Confocal microscopy experiment performed as in A, assessing the co-localization between
8 CERT and TGN46 in control and VAPA-Glu12* fibroblasts. Measurements were performed on
9 50 cells for each condition with the mean values indicated by the black lines.

10 C) LDs in control and VAPA-Glu12* fibroblasts were stained with BODIPY and imaged using
11 confocal microscopy.

12 D) Cholesteryl ester (CE), triacylglycerol (TG) and ether-linked triacylglycerol (TG[O]) were
13 measured by LC-MS from lipid extracts of control or VAPA-Glu12* fibroblasts. Boxplots show
14 average (colored point) and median (black line) from 4 independent experiments.

15 E) Confocal images of RPE1 WT or VAPA KO, as well as control or VAPA-Glu12* fibroblasts
16 stained with Mitotracker red. Scale bars : 20 μ m.

17 F) Automated quantification of mitochondrial morphology (form factor). Horizontal lines are
18 means of 3 independent experiments (500-3000 mitochondria analyzed per experiment).

19 G) Confocal images of endogenous OSBP and TGN46 visualized by immunofluorescence
20 staining in RPE1 cells KO for VAPA and transiently transfected for EGFP-VAPA or EGFP-
21 VAPA Δ 78. Cells surrounded by dotted lines show that the presence of VAPA WT but not Δ 78
22 rescues OSBP distribution.

23 H) Quantification of OSBP recruitment to the TGN. Horizontal lines are means from 3
24 independent experiments (~50 cells analyzed per condition).

25
26 **Figure 5 : VAPA and ABCA3 form a functional pair at ER-LB membrane contact sites**

1 A) Widefield images of A549 cells WT or KO for VAPA, transiently transfected for ABCA3-
2 mCherry WT, E690K or YF>AA, and pulse-chased with BODIPY FL C12-HPC.

3 B) WT or VAPA KO A549 cells were transiently transfected for ABCA3-mCherry, fixed,
4 stained for filipin and imaged to assess FC distribution using widefield microscopy.

5 C) Quantification of the cellular fraction of the BODIPY FL C12-HPC signal present in LBs,
6 from experiments described in A. Results are mean \pm SD from 3 independent experiments
7 (~45 cells analyzed per condition).

8 D) Quantification of the filipin signal measured in LBs as a percentage of total cellular signal,
9 from experiments described in B. Results are mean \pm SD from 4 independent experiments
10 (~60 cells analyzed per condition).

11 E) Alphafold2 model of the human ABCA3 structure. The two halves of ABCA3 are colored
12 light cyan and wheat. A cytosol-facing loop between TMD1 and NBD1, highlighted in purple,
13 was not resolved in the cryo-EM structures of ABCA3 (PDB IDs: 7W01 and 7W02), and is
14 designated here as intrinsically disordered region (IDR). This loop encompasses an FFAT
15 motif, shown as colored sticks.

16 F) Tau-STED imaging of A549 VAPA KO cells transiently transfected for HTN-VAPA WT or
17 HTN-VAPA Δ 78, and ABCA3-mCherry WT or YF>AA, labelled with Janelia Fluor 647 HaloTag
18 and fixed.

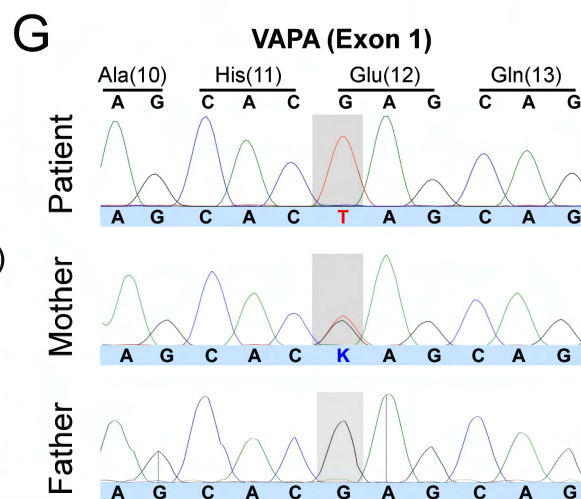
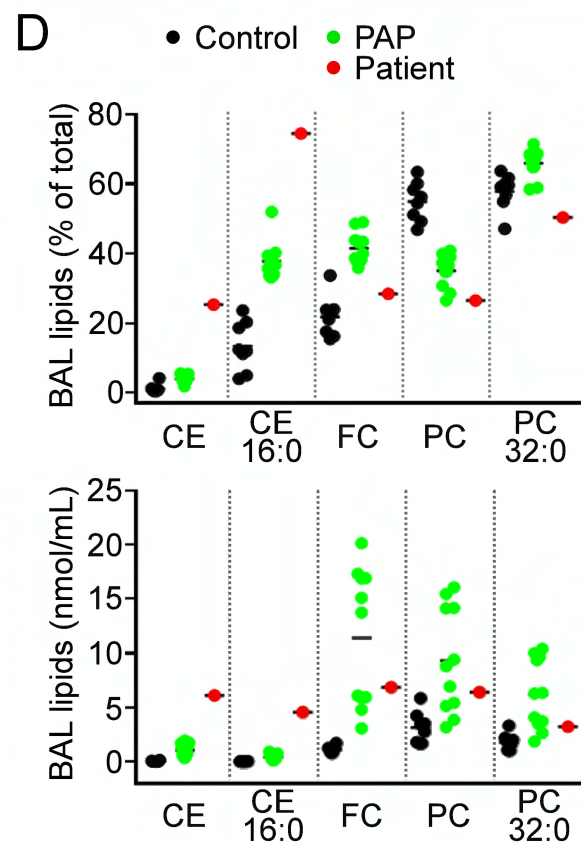
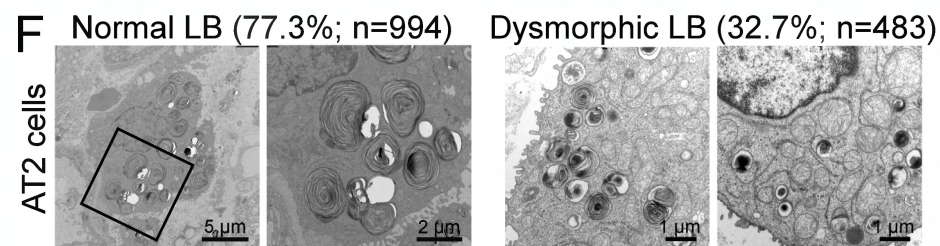
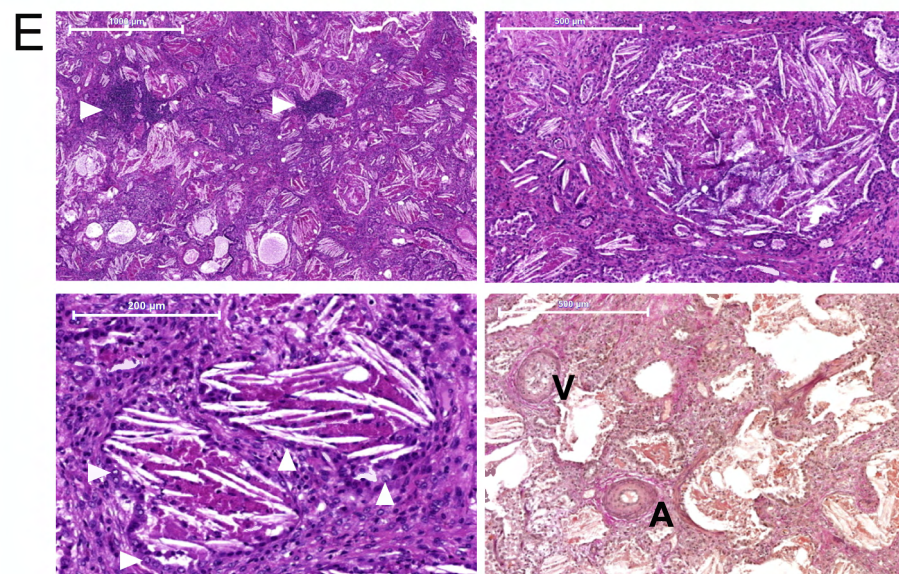
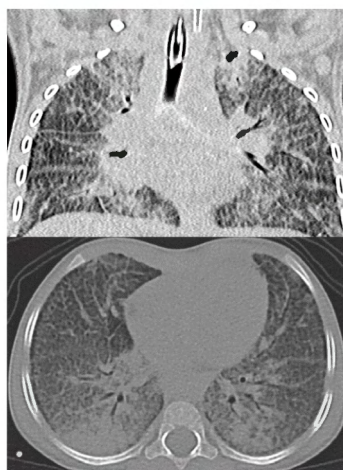
19 G) Widefield images of A549 VAPA KO cells transiently transfected for EGFP-VAPA WT or
20 Δ 78, together with ABCA3-mCherry WT or YF>AA, fixed and stained with filipin.

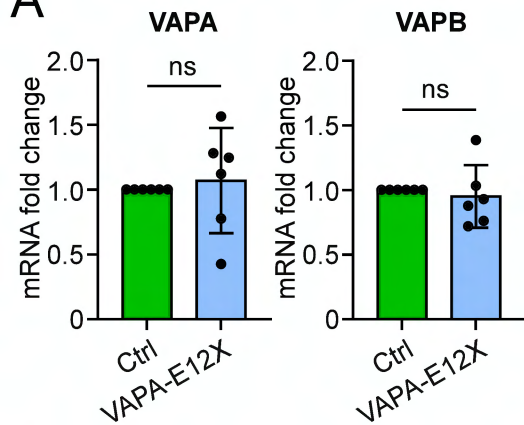
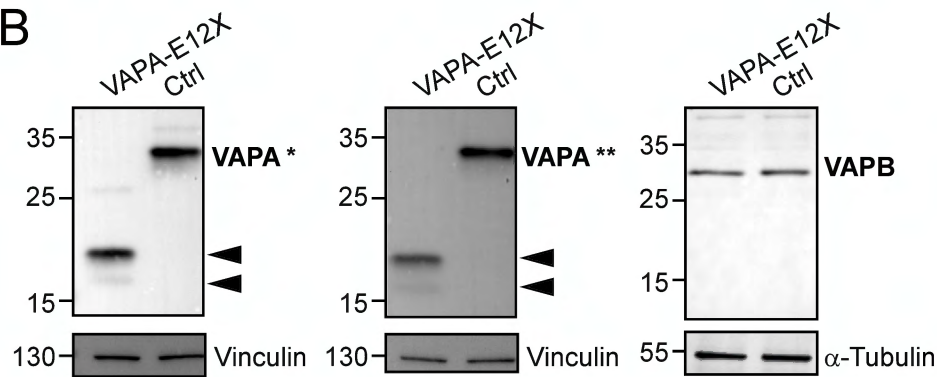
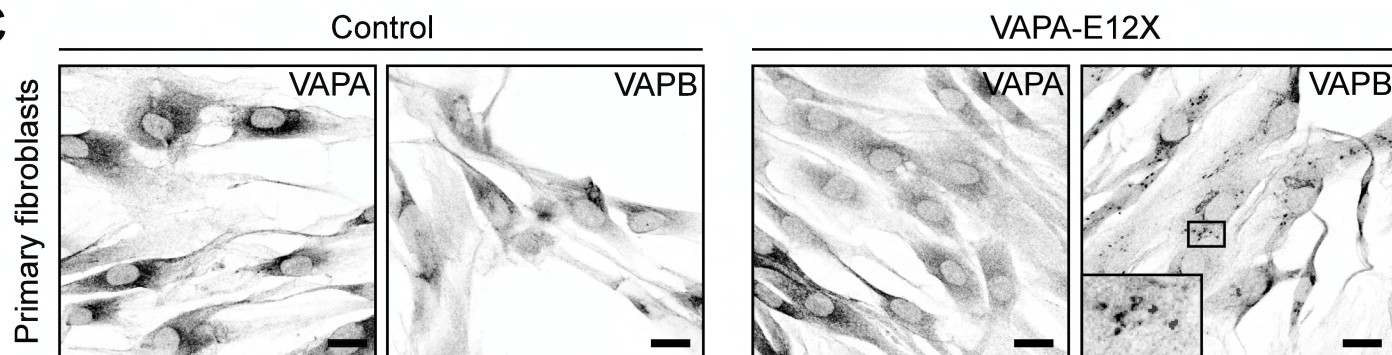
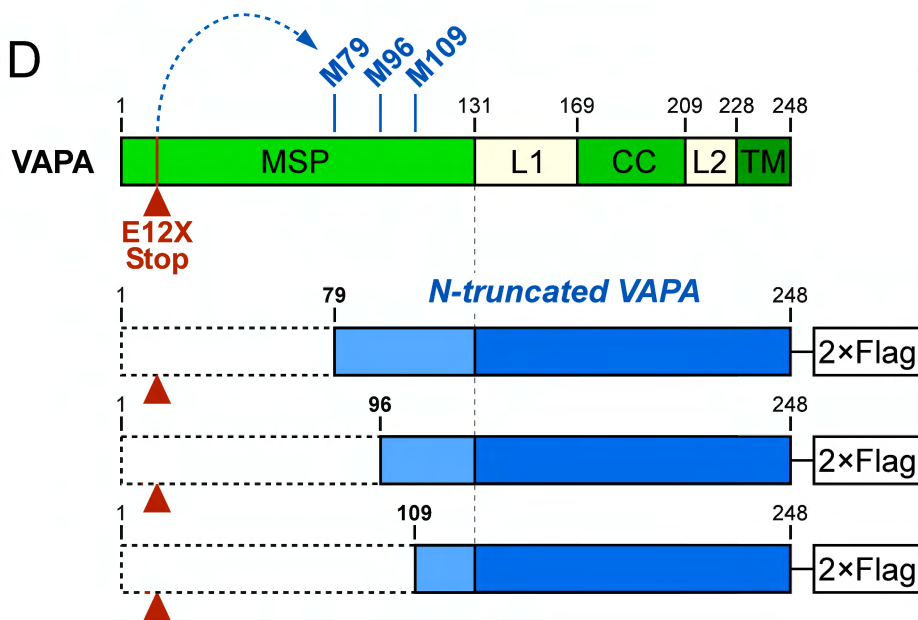
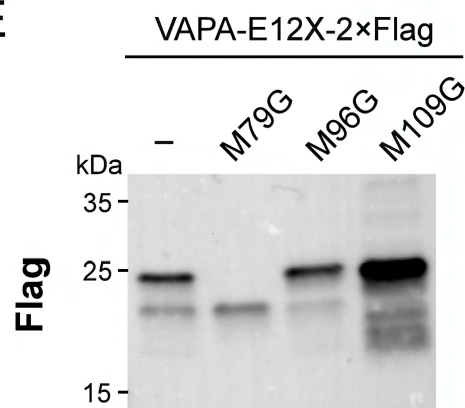
21 H) Quantification of the filipin signal measured in LBs as a percentage of total cellular signal,
22 from experiments described in G. Results are mean \pm SD from 4 independent experiments
23 (~30-50 cells analyzed per condition).

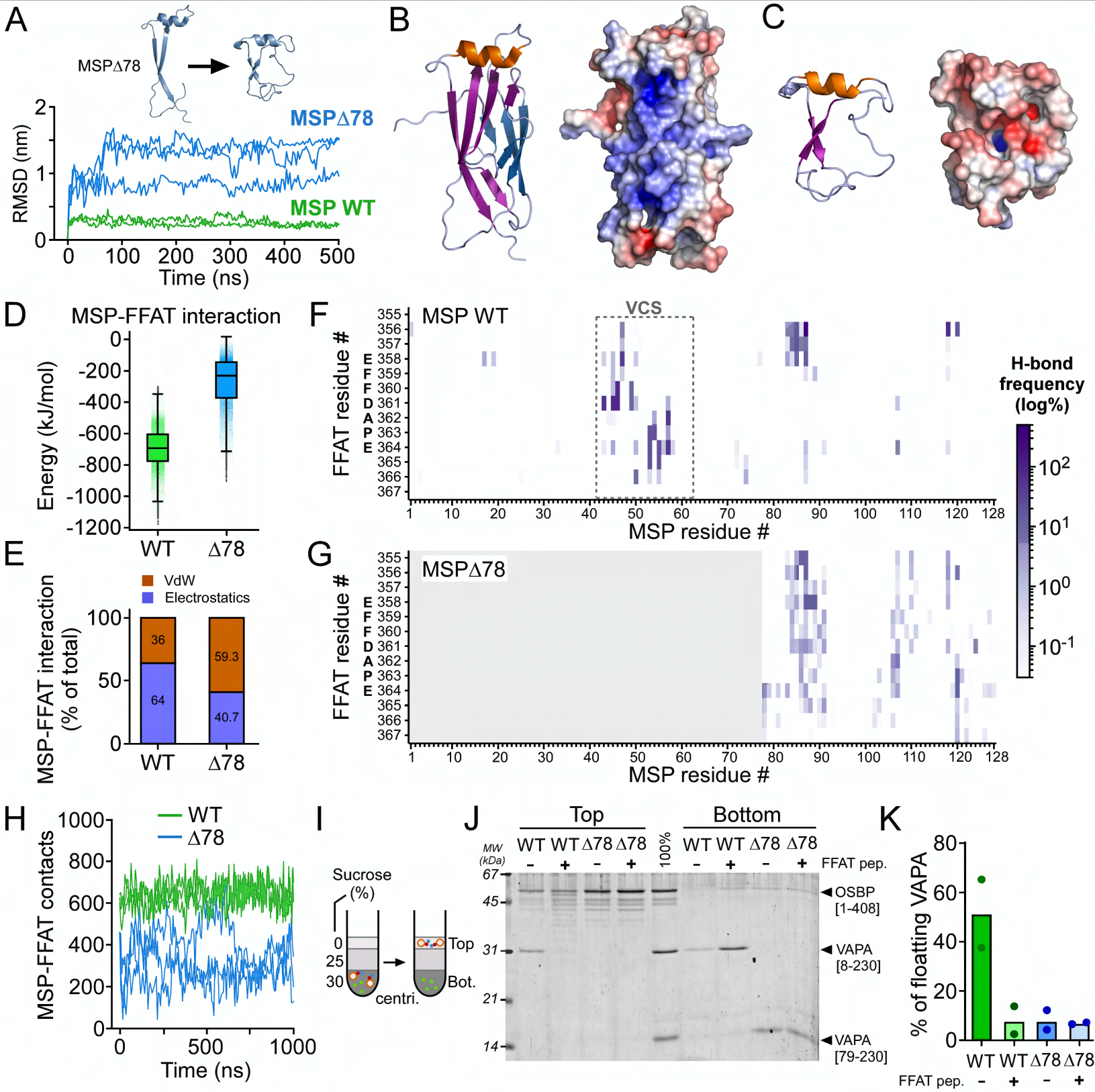
24 I) Model of the partnership between VAPA and ABCA3 at membrane contact sites for LB lipid
25 buildup, which is impaired in VAPA-Glu12* cells.

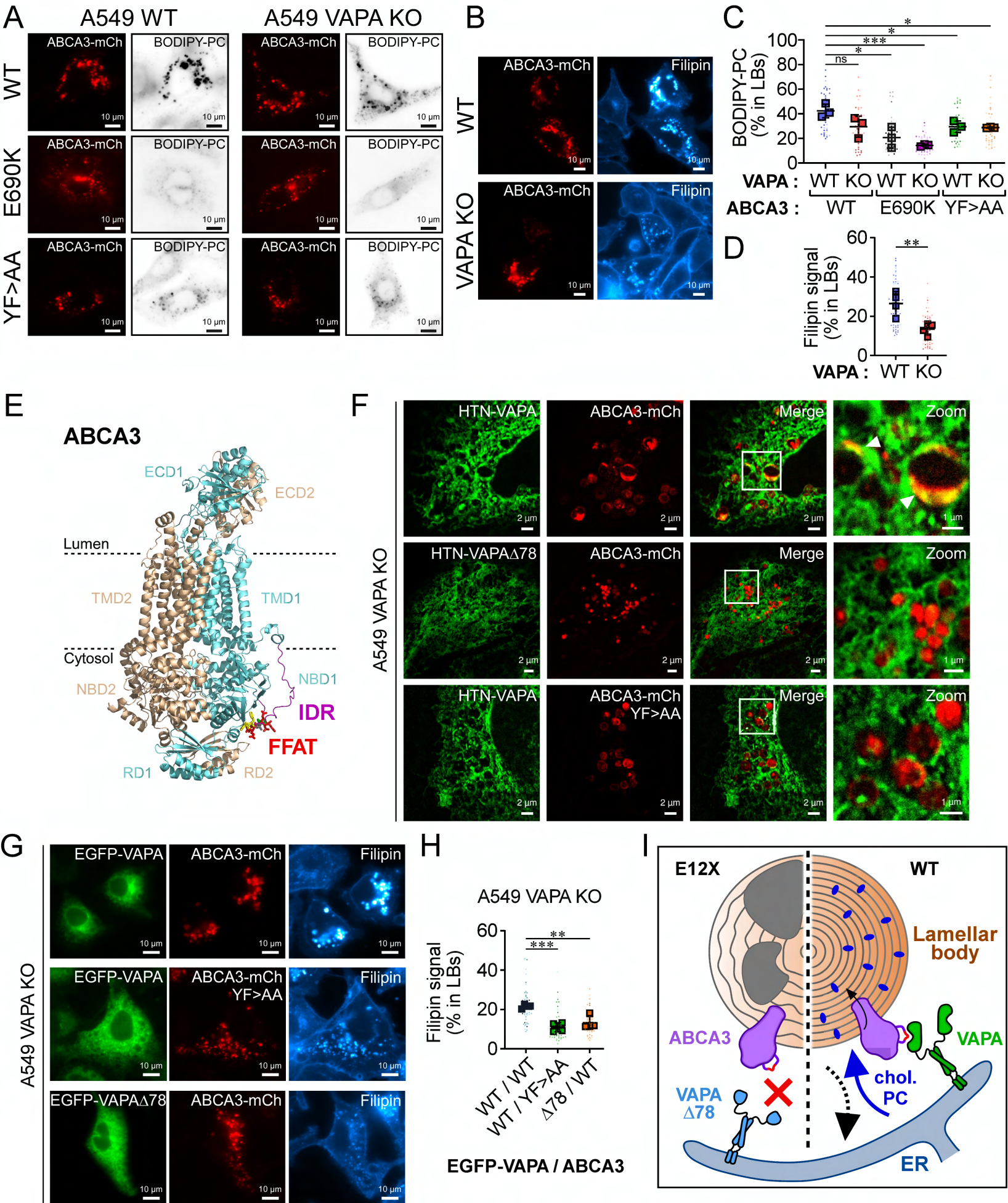
26

27



A**B****C****D****E**





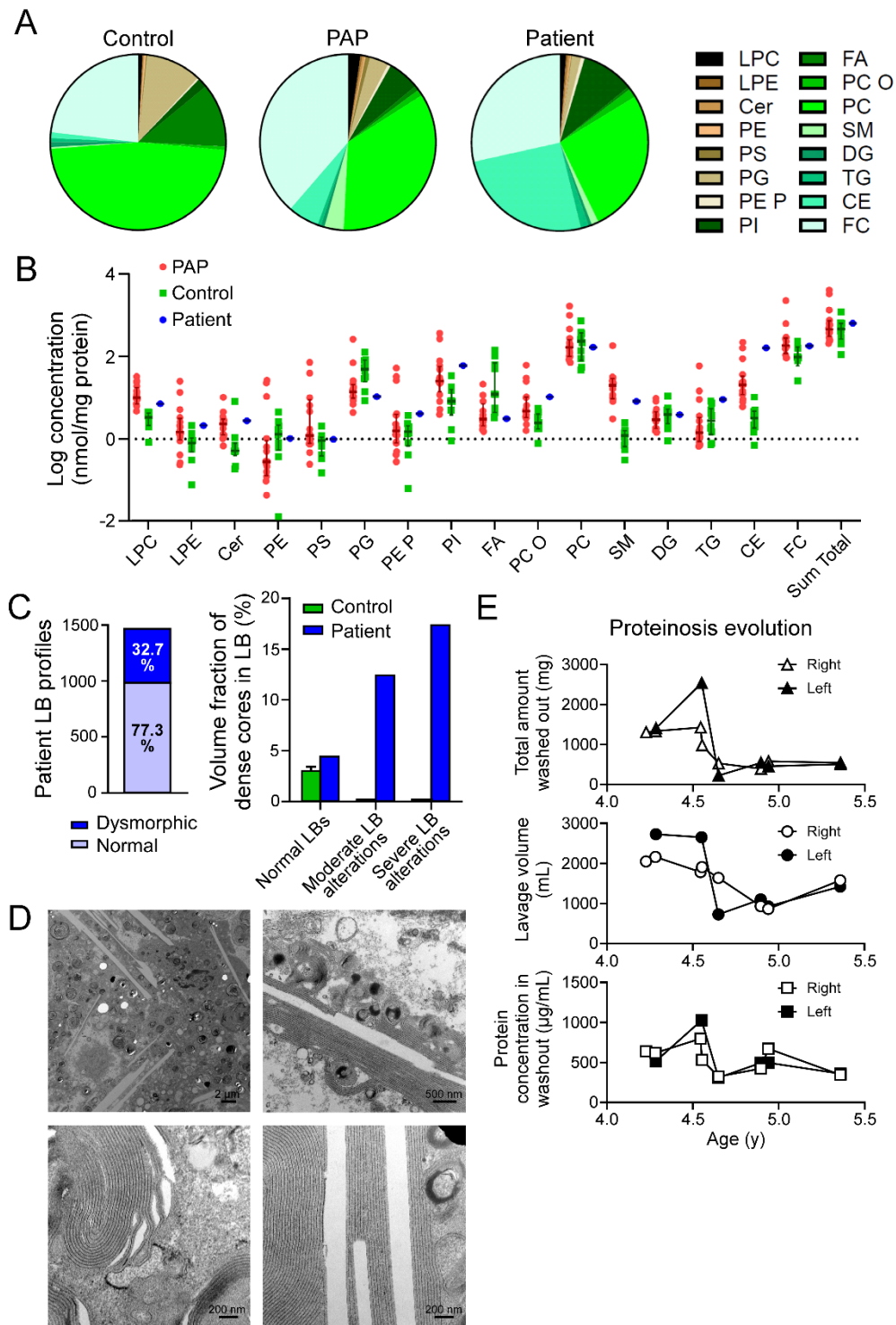


Figure S1. E12X patient BAL analysis and transmission electron microscopy of lung biopsy. Related to Figure 1.

(A) Analysis of BAL lipids of the patient compared to other PAP and controls. Pie charts show the different classes of lipids with the color code shown on the right side of the panel. Note the high proportion of CE in the E12X patient.

(B) Overview of the total concentration of BAL lipids of the patient compared to other PAP and controls.

(C) Quantification of LB morphology in lung samples from EM images. Left, E12X patient LB profiling. Right, analysis of the volume fraction of dense cores in LBs. 1477 LB profiles were assessed in 150 AT2 cells from 5 different lung samples from the E12X patient. Controls are from 3 “healthy” human lung samples (obtained from the Ewald Weibel collection).

(D) Transmission electron microscopy images of a lung biopsy from the E12X patient showing intra-alveolar lamellar protein/lipid material grouped around cholesterol crystals.

(E) E12X patient proteinosis evolution in relation to washed-out protein quantity upon whole lung lavages. Data from left and right lungs are presented.

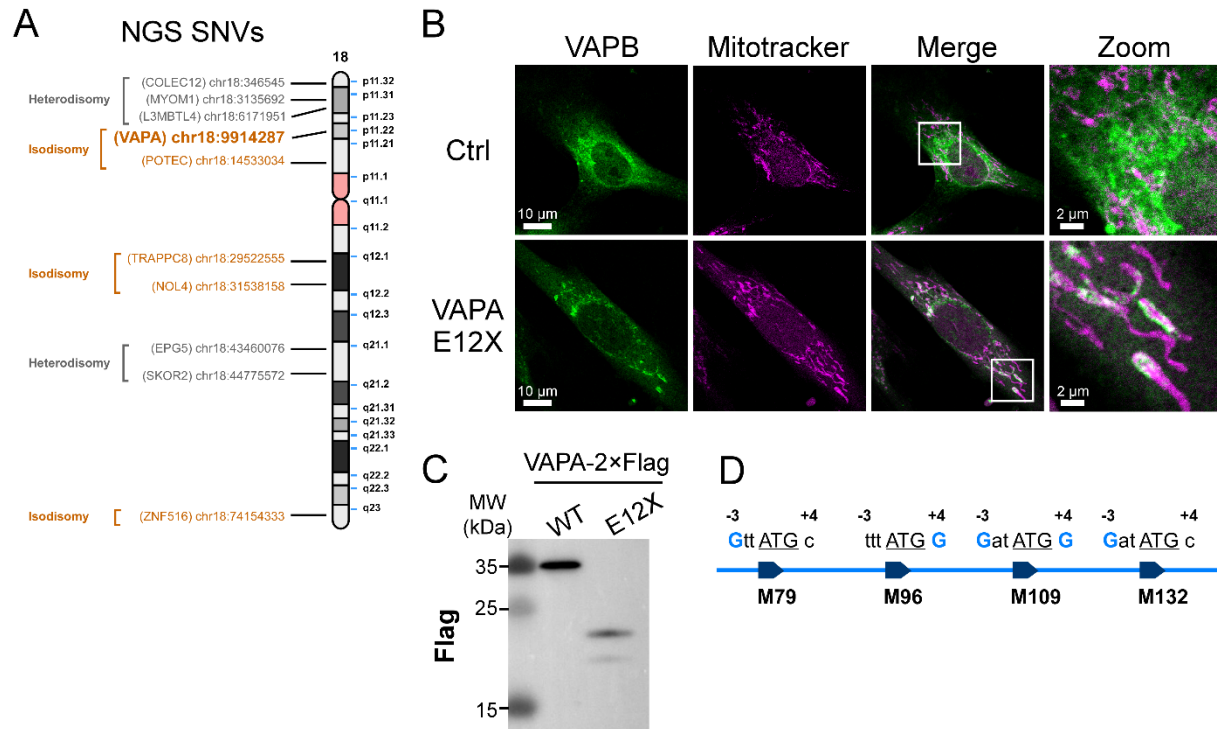


Figure S2. Patient chromosome analysis and characterization of the VAPA E12X molecular and cellular phenotype. Related to Figure 2.

(A) Single-nucleotide variants (SNVs) identified using Next-Generation Sequencing (NGS). Within the chromosome areas 18p11.22-18q12.1, isodisomy was detected for the *VAPA* variant and all other variants in homozygosity. These results correspond to a segmental maternal uniparental disomy 18p (mUPD 18p).

(B) Mitotracker labeling and immunofluorescence staining of VAPA in control and VAPA-E12X primary fibroblasts. VAPB is recruited to ER subdomains making close contacts with mitochondria in VAPA-E12X fibroblasts.

(C) Expression of VAPA WT and VAPA-E12X variant with an attached Flag tag in RPE1 WT cells analyzed by western blot. Note that the actual molecular weights differ from those of endogenously expressed proteins due to the 2xFlag tag, which accounts for about 4-5 kDa.

(D) Schematic representation of the Kozak context of alternative downstream start codons. Underlined ATG are in-frame start codons, with bold blue letters indicating conserved bases at positions -3 and +4.

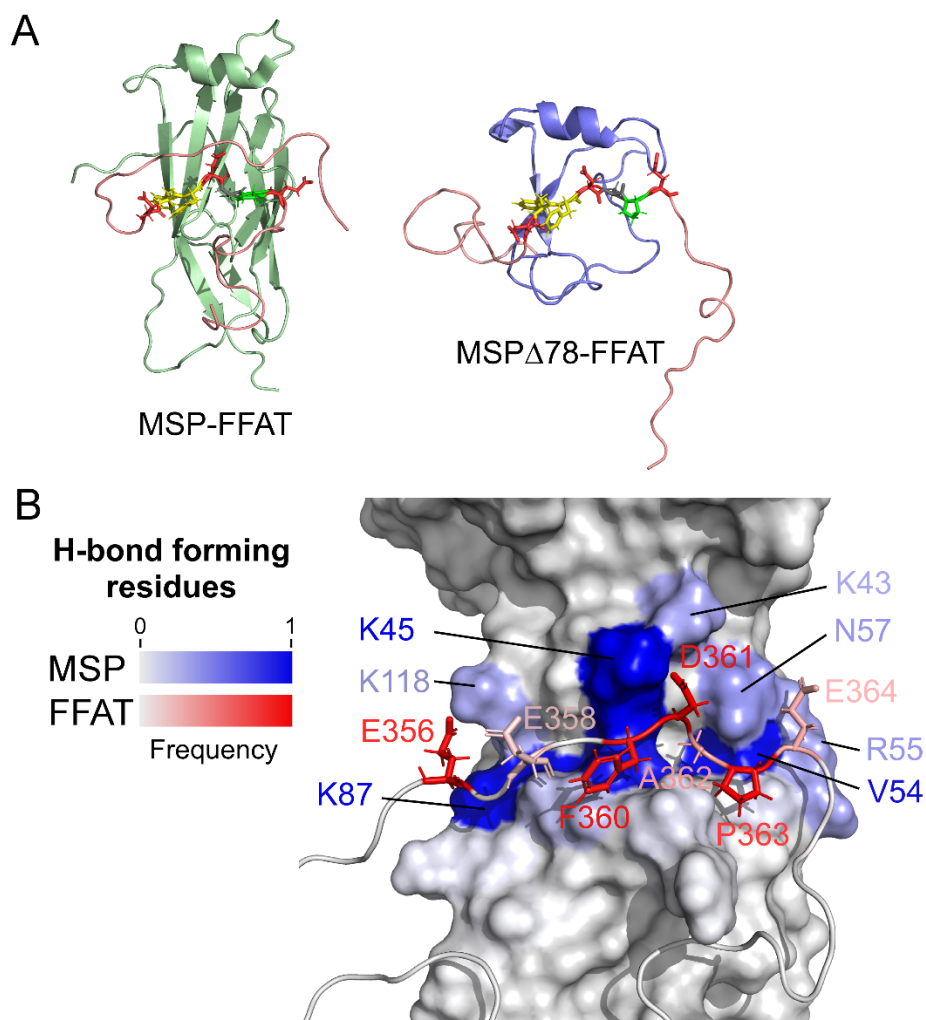


Figure S3. Molecular dynamics simulation analysis of VAPA MSP WT or MSP Δ 78 binding to FFAT. Related to Figure 3.

(A) Initial conformations of the complexes between MSP WT (green) or MSP Δ 78 (blue) and OSBP FFAT used for MD simulations. FFAT residues EFFDAPE are shown in colored sticks.

(B) Close-up view of the most representative conformation of the FFAT motif interacting with VAPA MSP WT, as obtained from simulation clustering. H-bond forming residues are color-coded (from grey to blue for MSP, or from grey to red for FFAT) as a function of H-bond frequency during simulation.

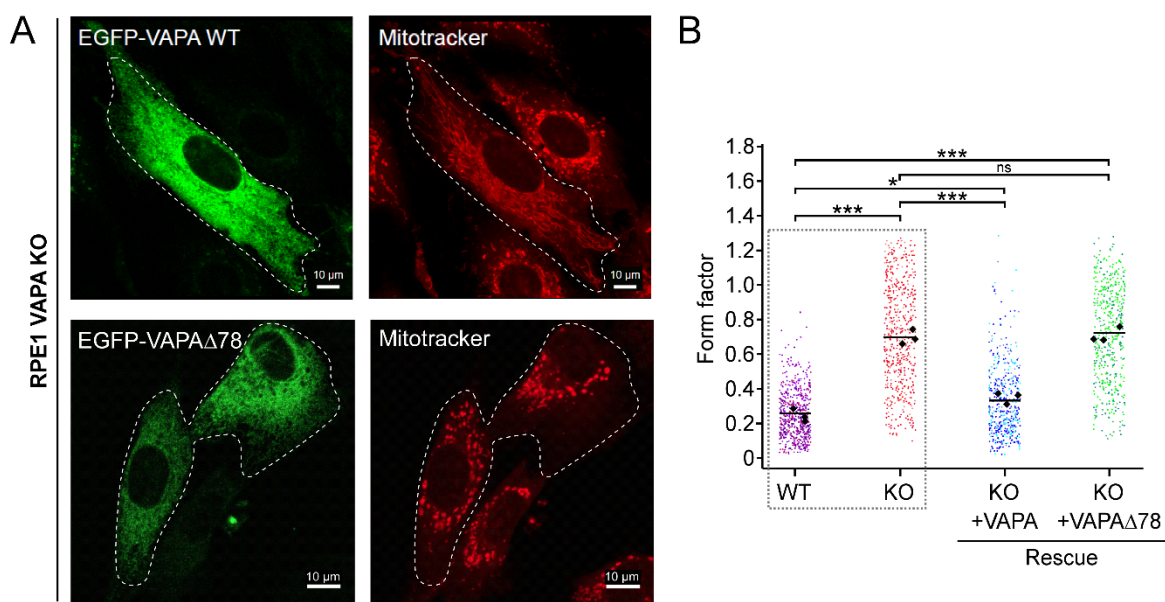
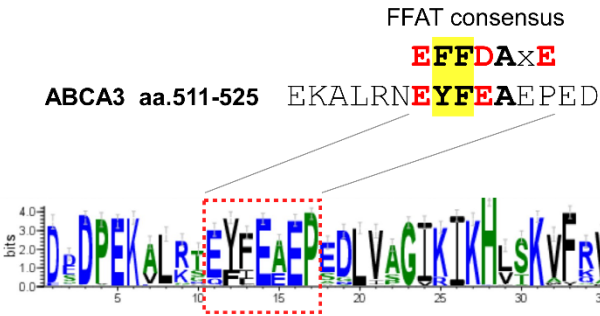


Figure S4. Rescue experiments assessing mitochondria morphology. Related to Figure 4.

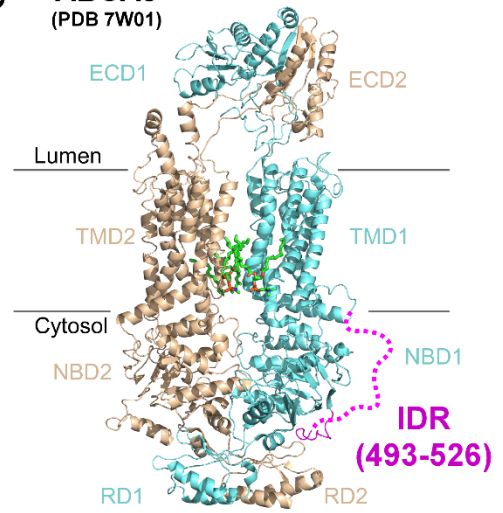
(A) Confocal images of RPE1 VAPA KO transiently transfected for EGFP-VAPA or EGFP-VAPA Δ 78 and stained with Mitotracker red. Cells surrounded by dotted lines show that the expression of EGFP-VAPA, but not EGFP-VAPA Δ 78, rescues mitochondria elongated shape.

(B) Automated quantification of mitochondrial morphology (form factor). Horizontal lines are means of 3 independent experiments (500-3000 mitochondria analyzed per experiment). The data in the dotted rectangle are the same as in Figure 4F (RPE1 WT and KO conditions) and are included here for comparison.

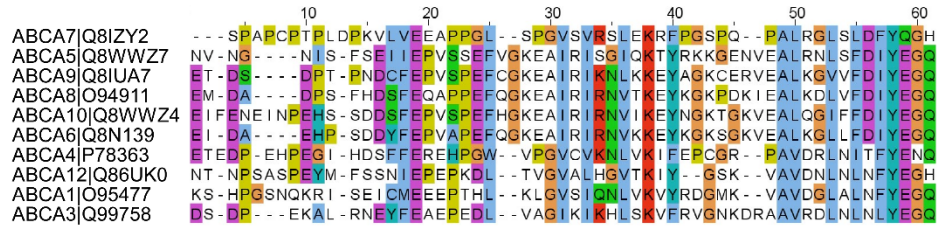
A



C

ABCA3
(PDB 7W01)

B



D

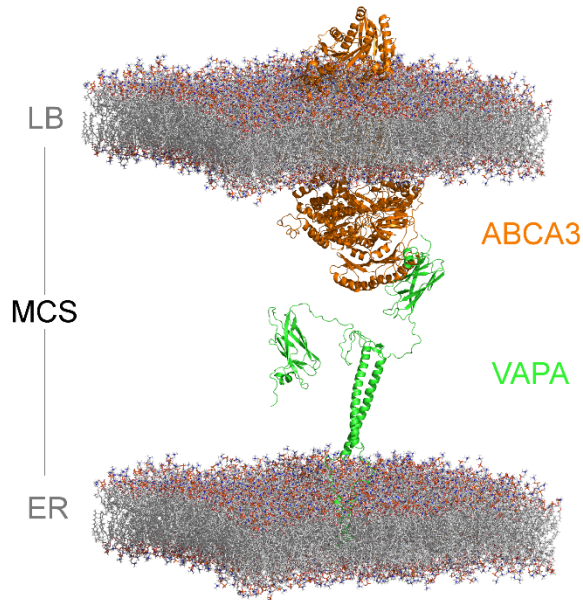


Figure S5. Sequence analysis of the ABCA3 FFAT motif and structural model for ABCA3-VAPA interaction at ER-LB contact sites. Related to Figure 5.

(A) Top, ABCA3 FFAT-like motif in comparison with the consensus FFAT motif. Bottom, WebLogo plot obtained from a PSI-BLAST search on the region spanning residues 507-560 of human ABCA3 FFAT, using the top 100 hits (66-100% sequence identity) to assess residues conservation.

(B) Multiple sequence alignment of human ABCA proteins generated using MUSCLE.

(C) Cryo-EM structure of ABCA3 (PDB 7W01). The two halves of ABCA3 are colored light cyan and wheat. A cytosol-facing loop (IDR) between TMD1 and NBD1, highlighted in purple, was not resolved. Lipid molecules resolved between the two TMD regions are shown in sticks.

(D) Putative domain organization of ABCA3 and VAPA interacting together at the interface between two membranes. This model aims to show protein domains at scale, thus suggesting distance between apposed membranes, here ~17-19 nm. The structural model takes into account the fact that VAPA is a flexible protein that can extend its length and interacts with the FFAT motif of ABCA3 via one of its MSP domains.